Novel computational fluid dynamics-finite element analysis solution for the study of flexible material wave energy converters 🔵EP

View Online   Export Citation   CrossMark

Yang Huang (黄扬),[1] 🔵 Qing Xiao (肖清),[1,a] 🔵 Guillermo Idarraga,[2] 🔵 Liu Yang (杨柳),[2] 🔵 Saishuai Dai (戴赛帅),[1] 🔵
Farhad Abad,[1] 🔵 Feargal Brennan,[1] 🔵 and Saeid Lotfian[1] 🔵

AFFILIATIONS

[1] Department of Naval Architecture, Ocean and Marine Engineering, University of Strathclyde, Glasgow, United Kingdom
[2] Advanced Composite Group, Department of Mechanical and Aerospace Engineering, University of Strathclyde, Glasgow, United Kingdom

Note: This paper is part of the special topic, Recent Advances in Marine Hydrodynamics.
a) Author to whom correspondence should be addressed: qing.xiao@strath.ac.uk

ABSTRACT

The use of flexible materials for primary mover and power takeoff of wave energy converters (WECs) has attracted considerable attention in recent years, owing to their potential to enhance the reliability, survivability, and wave energy conversion efficiency. Although some reduced order models have been used to study the fluid–structure interaction (FSI) responses of flexible wave energy converters (fWECs), they are somehow inappropriate due to their limited accuracy and applicability span. To gain a deeper understanding of the physical mechanisms in fWECs, a high-fidelity approach is required. In this work, we build up a fluid–structure interaction analysis framework based on computational fluid dynamics and a finite element analysis method. The incompressible viscous flow is resolved by solving three-dimensional unsteady Navier–Stokes equations with a finite volume approach. The structure dynamics are solved by a finite element method, taking the nonlinear behavior of flexible material into consideration. A strong coupling strategy is utilized to enhance the numerical stability and convergence of the iterative process. We demonstrate the present FSI tool is able to provide rich flow field information and structural response details, such as the velocity, pressure, and structural stress distribution. This is illustrated through several case studies, including two types of fWECs. The unsteady wave–structure-interaction and the associated nonlinear phenomena are also accurately captured by this tool.

I. INTRODUCTION

The conventional wave energy converter (WEC) designs using a rigid-body system with mechanical turbine faces challenges of high loads and corrosion in the marine environment, resulting in premature fatigue failures and poor adaptability to the wave climate (Collins *et al.*, 2021). Recent developments in the WEC design have shifted toward flexible bodies made of elastomeric composites, which can change their shape to accommodate the external loading and transfer the wave energy through an internal working fluid to the mechanical power takeoff (PTO). Additionally, dielectric elastomer generators (DEGs) can be integrated into stretchable materials; thus, such WEC design is greatly simplified by merging the primary mover and PTO. Compared to conventional rigid WECs, flexible wave energy converters (fWECs) exhibit superior performance in addressing reliability and

survivability issues while achieving higher energy conversion efficiency (Sirigu *et al.*, 2020; Zhang *et al.*, 2021).

A variety of fWECs with different shapes and operating mechanisms have been proposed to advance the development of wave energy. This includes oscillating water column (OWC) WEC [poly-A-OWC in Moretti *et al.* (2019; 2020)], flexible tube WECs [Anaconda and SBM S3 from Farley and Rainey (2011), Chaplin *et al.* (2012), Jean *et al.* (2012), and Babarit *et al.* (2017)], pneumatic cell based fWECs [AWS III and Bombora mWave from AWS (2023) and Leighton *et al.* (2021)], etc.

A series of wave tank tests and sea trials are conducted to investigate the hydro-elastic responses and power generation performance of these fWEC designs (Chaplin *et al.*, 2015; Algie *et al.*, 2016). Numerical analysis has also been applied in parallel to the research

and design of fWECs. The response of fWEC in waves is a highly complex fluid–structure interaction (FSI) problem, requiring multidisciplinary technologies, such as fluid mechanics, structural dynamics, and flexible material mechanics. The first attempt to analyze this FSI phenomena is to use so-called reduced order models, in which a linear potential flow theory with a boundary element method is used to solve the surrounding flow, and a modal analysis approach to determine the structure deformation (Farley et al., 2012; Algie et al., 2017; Kurniawan et al., 2017; Rosati Papini et al., 2018; McDonald et al., 2018; 2019; Moretti et al., 2019; 2020; Ancellin et al., 2020; Kelley et al., 2022; Kelly et al., 2022; and Shabara and Abdelkhalik, 2023).

Farley et al. (2012) proposed a one-dimensional dynamic model using potential flow theory and tube distensibility equations to study Anaconda WEC. Accurate predictions of bulge waves inside flexible tube can be made after considering the influence of surrounding water loading and PTO's impedance. Rosati Papini et al. (2018) and Moretti et al. (2019; 2020) developed a coupled analysis model by combining the nonlinear potential-flow hydrodynamics and electro-hyper-elastic theory. This model was utilized to design and evaluate a DEG-based fWEC. The work of McDonald et al. (2018; 2019) built up a generalized modeling tool for fWECs analysis. A quasistatic finite element analysis is integrated with a dynamic analysis in the frequency domain. On the basis of this tool, a software named Wave Venture TE^{TM} was further developed (Wave Venture Ltd., 2023). Moreover, Kelley et al. (2022) developed an open-source software WEC-Sim in MATLAB/SIMULINK for simulating WECs, which can model devices with hydrodynamic bodies, joints, constraints, PTOs, and mooring systems. Using this software, Kelley et al. (2022) examined the performance of flexible inflatable absorbers in contrast to rigid counterparts within a small-scale heaving WEC. Shabara and Abdelkhalik (2023) proposed a dynamic model employing a Lagrangian approach for a spherical variable-shape buoy (VSB) WEC. This model was integrated with the open-source boundary element method software NEMOH to explore the influence incorporating a flexible shape buoy on the trajectory and power generation of the WEC. The above reduced order models are characterized by fast computation speed. Therefore, they are widely used at the early design stage of fWECs.

However, due to the inherent strong nonlinearity and unsteady flow phenomena in the fluid–structure interaction system with large interface displacements, the accuracy of the reduced order model is highly limited. High-fidelity FSI models, which require directly solving the governing equations for both fluid and solid fields while accounting for the strong coupling between structure and fluid, is becoming a new approach. Within this framework, the Computational Fluid Dynamics (CFD) method with finite volume approach is used to model the surrounding flow, and the Finite Element Analysis (FEA) method is employed to obtain the structure dynamics (Dettmer and Perić, 2006; Bazilevs et al., 2013).

The higher fidelity CFD-FEA can model time-dependent wave–structure-interaction dynamics which cannot be captured by the reduced order model. However, it is computationally more expensive due to the high cost associated with the large number of meshes imposed around the structure. Additionally, how to deal with the moving boundaries associated with dynamic motion of device remains one of the modeling challenges. Commonly used method allows continuous deformation of the mesh while maintaining mesh topology unchanged (Ryzhakov and Oñate, 2017). The advantage of this

method is that the FSI interface can preserve a good mesh quality throughout the simulation, but the large deformation may lead to a grid distortion. Another approach is the immersed boundary method, which allows for the mesh topology alteration, thus is deemed more flexible to handle complex geometries (Dettmer et al., 2016; Kadapa et al., 2018). However, the imposition of boundary conditions inside the mesh, and the stabilization of cut cells increase computational difficulty and cost.

The nonlinear behavior of flexible materials is another challenge for the CFD-FEA model. Usually, the materials used for fWECs are mostly hyper-elastic, such as natural rubber, styrene-butadiene rubber, exhibiting strong nonlinear stress–strain characteristics. Although a variety of hyper-elastic models are available to describe nonlinear material properties, such as Mooney–Rivlin (Mooney, 1940; Rivlin, 1948) and Yeoh (Martins et al., 2006), an appropriate hyper-elastic model with the model parameters to be determined from material mechanical property tests is needed to accurately model the structural dynamics of fWEC. The coupling strategy between the fluid flow solver and material structure solver is also a key issue. Partitioned solution schemes exchange data across the interface boundary and use separated fluid and structural solvers. These methods are computationally efficient but can be challenging with regard to numerical stability (Farhat et al., 2010; Dettmer et al., 2021). On the other hand, monolithic solution schemes solve the fluid-solid system of equations as a single coupled system, resulting in improved accuracy but requiring a more computationally intensive approach (Dettmer and Perić, 2006; Ryzhakov and Oñate, 2017).

Due to the aforementioned complexities, there are very few successfully high-fidelity simulations of fWECs. King et al. (2016) used a coupled CFD-FESI model to study the Bombora WEC. In their model, OpenFOAM was selected to solve the incompressible flow, and a simplified finite element model without considering the inertia term was used to obtain the membrane deformation. In addition, Zou and Abdelkhalik (2021) and Shabara et al. (2021) both used ANSYS two-way FSI approach successfully simulated the dynamic responses of a VSB WEC.

In this study, we establish a fully coupled FSI analysis tool based on the CFD-FEA method, which provides a powerful numerical analysis tool for simulating the FSI problems of fWECs. With this tool, detailed flow field information, dynamic response of flexible structures, nonlinearity of waves, and nonlinear behavior of flexible materials can all be obtained. These results will offer valuable insights for enhancing the design of fWECs. Several FSI problems are first modeled to demonstrate the accuracy and robustness of the established tool, then this tool is applied to the modeling of two types of fWECs in regular waves.

The remainder of this article is organized as follows: we introduce the establishment of FSI analysis tool including the fluid solver, structure solver, and coupling approach in Sec. II. Several FSI problems involving waves, hyper-elastic materials, and fWECs are studied, with an analysis of the associated case study results in Sec. III. Discussions and conclusions will be presented in Sec. IV.

II. FSI ANALYSIS TOOL

Several FSI tools at different levels of complexity have been built up in our previous studies for the fluid–flexible-structure interaction problems. For example, Liu et al. (2017) combined open-source CFD

toolbox OpenFOAM (Jasak *et al.,* 2007) with multibody dynamics analysis software MBDyn (Masarati *et al.,* 2003) to investigate the aeroelastic response of floating offshore wind turbine with flexible blades. This tool was also applied to the modeling of a mechanically coupled WEC array and a floating offshore wind turbine subjected to focused waves (Zhou *et al.,* 2021; Li *et al.,* 2022). To consider more complex material and structural characteristics, such as the hyper-elastic material and non-uniform stiffness distribution of flexible structure, Luo *et al.* (2020c) developed another CFD-FEA based FSI analysis tool for its application in bio-inspired fish swimming analysis (Luo *et al.,* 2020c; Luo *et al.,* 2020a; and Luo *et al.,* 2020b). In that tool, an in-house CFD solver is coupled with an open-source three-dimensional (3D) FEA code CalculiX (Dhondt, 2017) via an open-source library preCICE (Bungartz *et al.,* 2016). The present numerical modeling tool for flexible WEC investigation is a further development from the foundations mentioned above, an integration of OpenFOAM, CalculiX, and preCICE. Some preliminary studies in fWECs area can be found from the papers by Li and Xiao (2022) and Huang *et al.* (2023). More details will be presented in this section.

A. Fluid solver

1. Governing equations

To predict the flow field around the fWEC, two-phase incompressible viscous flows are solved by the fluid solver. The governing equations are defined by the following equations:

$$\nabla \cdot \mathbf{u} = 0, \tag{1}$$

$$\frac{\partial (\rho \mathbf{u})}{\partial t} + \nabla \cdot (\rho (\mathbf{u} - \mathbf{u}_g))\mathbf{u}$$
$$= -\nabla p_d - \mathbf{g} \cdot x \nabla \rho + \nabla \cdot (\mu \nabla \mathbf{u}) + (\nabla \mathbf{u}) \cdot \nabla \mu + f_\sigma + f_s, \tag{2}$$

where all the bold letters indicate a vector field, $\mathbf{u}$ is the flow velocity, $\mathbf{u}_g$ is the velocity of mesh grid, induced by the dynamic mesh, $\mathbf{g}$ is the gravity acceleration, ρ denotes the mixture density of the air and water phases, p_d is the pseudo-dynamic pressure, μ is the dynamic viscosity, f_σ represents the surface tension term, and f_s is the source term generated by the porous media, which will be discussed in Sec. III D 2.

The volume of fluid (VOF) method is adopted to capture the free surface (Berberović *et al.,* 2009). In order to describe the movement of the air and water phases, the following transport equation is required:

$$\frac{\partial \alpha}{\partial t} + \nabla \cdot (\mathbf{u}\alpha) + \nabla \cdot [\mathbf{u}_c \alpha (1 - \alpha)] = 0, \tag{3}$$

where α is an indicator phase function that defines the quantity of water per unit of volume at each cell, $\nabla \cdot [\mathbf{u}_c \alpha (1 - \alpha)]$ is called artificial compression term, used to maintain a sharp interface and make α conversion (Weller, 2002). $|\mathbf{u}_c| = \min[c_\alpha |\mathbf{u}|, \max(|\mathbf{u}|)]$. c_α is a constant that denotes the compressibility of fluid.

The fluid solver uses the finite volume approach to discrete the above governing equations in fluid domain. The PIMPLE algorithm is employed to for pressure–velocity coupling (Jasak, 1996). It is noted that the fluid solver provides a variety of turbulence models, including one-equation and two-equation models, while this work uses the laminar flow to simulate low Reynolds number flows in all case studies.

2. Wave generation and absorption

An accurate wave generation is critical for the FSI simulation of fWECs. In the fluid solver, several boundary conditions are coded based on OpenFOAM to generate various regular and irregular waves. According to the selected wave theory and wave parameters, we can obtain the free surface and velocity at the inlet boundary. For instance, the free surface (η) and velocity components (u, v, w) are given by Eqs. (4) and (5) when Stokes 1st order wave theory is selected (Dean and Dalrymple, 1991),

$$\eta = \frac{H}{2} \cos(k_x x + k_y y - \omega t + \psi), \tag{4}$$

$$\begin{cases} u = \frac{H}{2} \omega \dfrac{\cosh[k(h + z)]}{\sinh(kh)} \cos(\theta)\cos(\beta), \\ v = \frac{H}{2} \omega \dfrac{\cosh[k(h + z)]}{\sinh(kh)} \cos(\theta)\sin(\beta), \\ w = \frac{H}{2} \omega \dfrac{\sinh[k(h + z)]}{\sinh(kh)} \sin(\theta), \end{cases} \tag{5}$$

where H is the wave height, $\omega = 2\pi/T$, in which T is the wave period, ψ is the initial wave phase, β represents the direction of wave propagation, k is the wave number, k_x and k_y are the components of k, calculated by $k_x = k\cos(\beta)$ and $k_y = k\sin(\beta)$, h is the water depth, θ is the total phase angle, and x, y, and z denote the coordinates of the given point in flow field.

To avoid wave reflections at the boundary and eliminate its impact on the hydrodynamic calculations, it is necessary to consider the absorption of waves. There are two widely applied wave absorption methods, i.e., relaxation zones and active wave absorption. In most of our previous work, the relaxation zones were used to absorb the reflected waves (Liu *et al.,* 2019; Zhou *et al.,* 2019; 2021). However, this technique leads to an increase in the mean water level and requires a large computational domain and a high number of grids, resulting in higher computational costs (Wei and Kirby, 1995). The active wave absorption technique in the simulation of a WEC array proved that it can directly absorb the waves at boundaries and has no impact on the water level in the computational domain (Li *et al.,* 2022). Therefore, in the present study, the active wave absorption approach is used based on olaFlow (Higuera *et al.,* 2014a; 2014b), which provides three different active wave absorption options, in order of applicability from small to large, i.e., 2D, quasi-3D (Schäffer and Klopman, 2000) and 3D (Higuera *et al.,* 2013). Given that the incident waves in the present study have an angle of $0°$, the 2D absorption approach adequately fulfills the computational demands. To nullify the reflected waves, the boundary must generate a velocity of equal magnitude but opposite direction to the incident waves, as specified by the following equation:

$$U_m = -\sqrt{\frac{h}{g}}\eta_r. \tag{6}$$

The correction velocity (U_m) is applied perpendicular to the boundary and directed toward the domain, ensuring the absence of reflections. The reflected wave height (η_r) is determined by subtracting the measured elevation at the wavemaker (η_m) from the desired target elevation (η_t), according to the expected reflection-free wave generation.

3. Mesh handling

In FSI simulations, flexible structures deform under the influence of time-dependent fluid forces, leading to the changes around the interface between fluid and structure. Therefore, the interface mesh in the fluid domain needs to be updated. A moving-mesh technique is employed to handle the mesh deformation. The topology of the mesh does not change when the interface deforms, but only the spacing between nodes changes by stretching and squeezing and cell shape deforms, as shown in Fig. 1. The relationships between adjacent mesh nodes, edges, and faces are preserved and do not undergo any modifications during the simulation process.

The position of the mesh points in fluid domain are obtained by solving a Laplace equation with variable diffusivity,

$$\nabla \cdot (\gamma \nabla X_g) = 0, \ \gamma = \frac{1}{r^2}, \tag{7}$$

where X_g is the displacement of mesh points obtained from the structural deformation and γ represents the diffusivity field, which varies quadratically with the inverse of the distance r between the cell center and the deformed interface. It means that the mesh points closer to the deformed interface will have smaller displacements, therefore ensuring good mesh quality after deformation.

B. Structure solver

1. Governing equations

The weak form of the balance of momentum written in differential form is chosen as the governing equation for the flexible structure,

$$\rho_s \frac{D\mathbf{v}}{Dt} = \nabla \cdot \mathbf{S} + \mathbf{f_b}, \tag{8}$$

where ρ_s is the density of structure, $\mathbf{v}$ represents the velocity vector of material point, $\mathbf{S}$ denotes the second Piola–Kirchhoff stress tensor, and $\mathbf{f_b}$ is the body force vector.

In order to have a set of closed-form equations, Eq. (9), an equation that relates stress and strain is required,

$$\mathbf{S} = \mathbf{C} : \mathbf{E}, \ \mathbf{E} = \frac{1}{2}(\mathbf{F}^T\mathbf{F} - \boldsymbol{\delta}), \tag{9}$$

where $\mathbf{C}$ is the elasticity tensor, $\mathbf{E}$ represents the Green–Lagrange strain tensor, the ":" symbol represents the contraction of two tensors, $\mathbf{F}$ denotes the deformation gradient, and $\boldsymbol{\delta}$ represents the unit tensor.

The finite element method is used to discretize the above structure governing equations. Based on the virtual work approach, Eq. (8) is discretized into the following algebraic equation system:

$$[M]\{\mathbf{a}\} + [C]\{\mathbf{v}\} + [K]\{\mathbf{x}\} = \{\mathbf{f}\}, \tag{10}$$

where $\{\mathbf{a}\}$, $\{\mathbf{v}\}$, and $\{\mathbf{x}\}$ represent the displacement, velocity and acceleration vectors, respectively, $[M]$, $[C]$, and $[K]$ denotes the global mass, damping and stiffness matrix, respectively, and $\{\mathbf{f}\}$ is the global force vector leading the structure deformation. In addition, the α-method is applied to discretize the time domain in the present structural analysis. A detailed description of its implementation can be found in Luo et al. (2020c).

2. Hyper-elastic model

The flexible materials used in the fWECs are mainly rubber-like polymeric materials, such as silicone, acrylic, polyurethanes, and natural rubbers, which exhibit substantial nonlinear stress–strain behavior. Recent experimental studies indicate that these materials typically possess viscoelastic properties, illustrated by a time-dependent behavior and energy dissipation over time (Liao et al., 2020; Collins et al., 2023). Obviously viscoelastic models offer the most suitable approach for accurately describing the mechanical characteristics of these materials. However, implementing viscoelastic models presents considerable challenges for our existing structural solvers. This involves modifications to constitutive equations and algorithms, as well as the introduction of additional parameters to account for time-dependent behavior. An acceptable alternative while with reasonable accuracy is to employ a hyper-elastic model to describe the nonlinear stress-strain behavior of materials while neglecting their time-dependent characteristics. This approach is acceptable and has been widely adopted in the study of fWECs (Rosati Papini et al., 2018; Moretti et al., 2019; 2020).

In our current structural solver, the viscoelastic model is not available, while it provides a variety of hyper-elastic models, including Mooney–Rivlin, Neo Hooke, Ogden, Polynomial, Yeoh, etc. (Steinmann et al., 2012; Anssari-Benam and Bucchi, 2021). In these models, the stress-strain relationship of the flexible material is derived from a strain energy density function. Taking the Yeoh model as an example, the material characteristics are defined by the following formula (Martins et al., 2006):

$$W = \sum_{i=1}^{n} C_{i0}(\bar{I}_1 - 3)^i + \sum_{k=1}^{n} C_{k0}(J - 3)^{2k}, \tag{11}$$
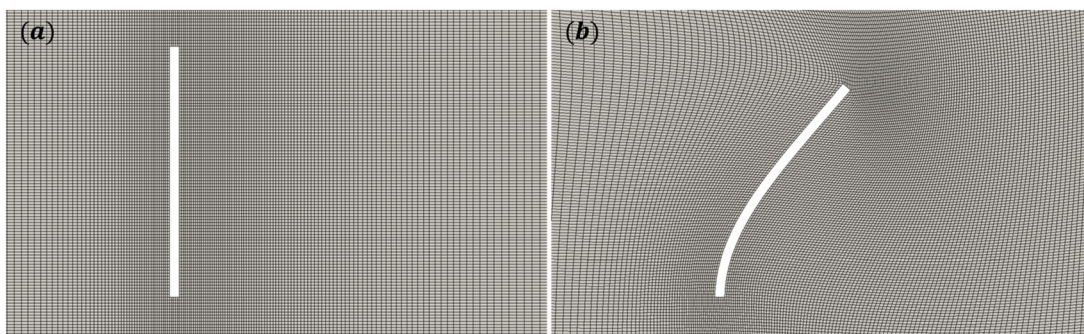

FIG. 1. Mesh deformation of a flexible plate using the moving-mesh technique: (a) initial mesh and (b) deformed mesh.

where W is the strain energy density, $\bar{I}_1 = J^{-2/3}I_1$ and $J^2 = I_3$, in which I_1 and I_3 are the strain invariants of the Cauchy–Green deformation tensors, and C_{i0} and C_{k0} are constants related to material properties. When $n = 1$, the compressible Yeoh model reduces to the Neo–Hookean model for incompressible materials.

The suitable hyper-elastic model varies for different hyper-elastic materials, and the corresponding hyper-elastic constants can be obtained by fitting the stress–strain curves obtained from material experiments, including uniaxial, planar, and biaxial tests.

C. Fluid–structure coupling

1. Coupling approach

To overcome the challenge of numerical instability in FSI problems, especially when fluid and structure densities are comparable (Causin *et al.*, 2005; Förster *et al.*, 2007; and Küttler and Wall, 2008), a strong coupling approach is selected in this study, which means that the fluid and solid are solved simultaneously and iteratively at each time step. Moreover, a partitioned coupling scheme is adopted to couple the fluid and structure, which offers several benefits such as the flexibility to choose different numerical techniques for each domain, scalability, and the capability to handle complicated geometries.

An implicit scheme is employed in the current FSI simulations to take larger time steps, while ensuring numerical stability and reducing computational cost. Two implicit coupling schemes, serial and parallel, are available in preCICE, corresponding to the staggered and parallel execution of the fluid and solid solver, respectively. Both schemes lead to the same physical results, as demonstrated in the study by Mehl *et al.* (2016). To improve the calculation efficiency, the parallel coupling is selected. In addition, an improved IQN-ILS method is implemented in preCICE is used to stabilize and accelerate the coupling iterations (Degroote *et al.*, 2009). A simplified solving procedure of the

FSI simulation adopting the implicit coupling scheme is presented in Fig. 2.

2. Data exchange

Due to different meshes of fluid and solid, data exchange between them is achieved through data mapping and interpolating at the interface. Before performing data exchange, specific adapters are required to process the data from fluid and structure and communicate with preCICE. In this work, the adapters developed by Chourdakis *et al.* (2023) and Uekermann *et al.* (2017) are designed for the fluid and solid solvers, respectively. An interpolation method based on radial basis function (RBF) is employed to transfer node forces from the fluid to the solid, and vertex displacements in the opposite direction (Lindner *et al.*, 2017). Two different mapping schemes, conservative and consistent, are implemented in the RBF interpolation. To ensure the energy balance over the interface, the conservative scheme that makes the sum of the data values in both sides equal is applied for the force mapping, while the consistent scheme is adopted for the displacement mapping (de Boer *et al.*, 2008).

3. Convergence criterion

To quantify the convergence of the partitioned coupling toward monolithic solution, the discrete l_2 norm of the difference of solutions between two adjacent iterations is calculated, given by the following formula:

$$\|\boldsymbol{r}_{k+1}\|_2 = \left(\sum_i^N r_{k+1,i}^2\right)^{1/2}, \tag{12}$$

where $\boldsymbol{r}$ denotes the residual vector, N is the dimension of $\boldsymbol{r}$, the subscripts i is the index of $\boldsymbol{r}$, and the subscripts k represents the interaction number.
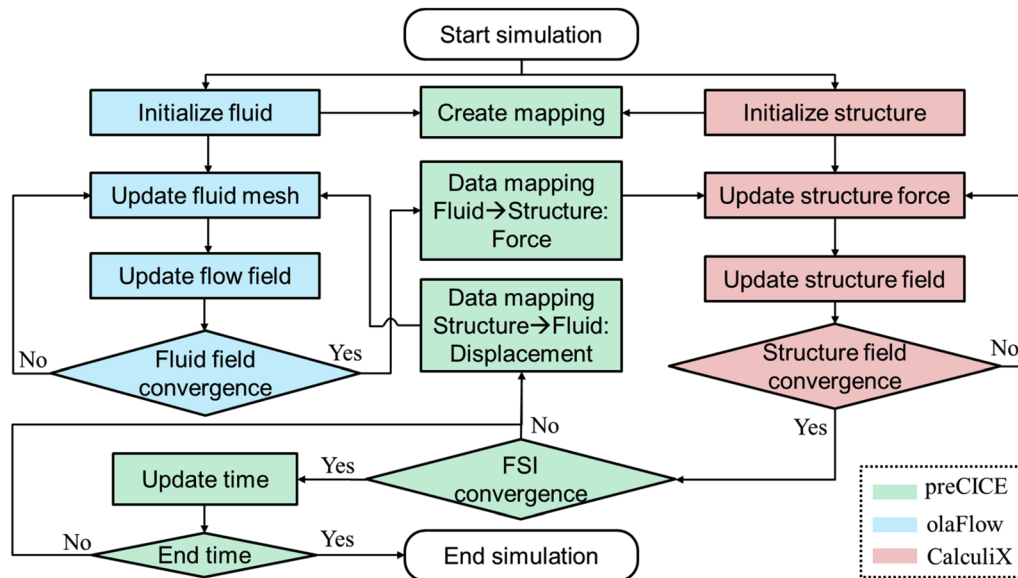

FIG. 2. Solving procedure of the FSI simulation adopting implicit coupling scheme.

In this work, a relative convergence criterion is selected to evaluate the convergence of the solutions, which is defined by

$$\frac{\|\boldsymbol{r}_{s,k+1}\|_2}{\|\boldsymbol{d}_k\|_2} < \varepsilon_{\mathrm{d}} \quad \text{and} \quad \frac{\|\boldsymbol{r}_{f,k+1}\|_2}{\|\boldsymbol{f}_k\|_2} < \varepsilon_{\mathrm{f}}, \tag{13}$$

where $\boldsymbol{d}$ and $\boldsymbol{f}$ represent the displacement and force vectors, respectively, ε_{d} and ε_{f} predefined convergence limit for the displacement and force, respectively. In each time step, the relative residual typically decreases as the number of sub-iterations increases. The sub-iterations will continue until the convergence criteria are met or the maximum iteration number is reached.

III. CASE STUDIES

Based on the established FSI analysis tool, we have investigated several fluid-flexible-structure interaction problems, including the bending of a 3D flexible plate in a uniform current and the deformation of a floating elastic disk in regular waves. To demonstrate the capabilities of this tool for the study of fWECs, we have simulated the flexible OWC WEC and flexible tube WEC in regular waves.

A. Case 1: Flexible plate in a uniform current

This topic is derived from an experimental study on the flow-induced reconfiguration of flexible aquatic vegetation (Abdelrhman, 2007; Luhar and Nepf, 2011). Numerical simulations have been previously conducted by Tian *et al.* (2014) and Luo *et al.* (2020c) at different Reynolds numbers.

1. Problem description

As shown in Fig. 3(a), an elastic plate of height h, width b and thickness t is vertically placed in a uniform crossflow. One end of the plate is fixed, while the other end is free. The dimensionless parameters are $h = 5b$ and $t = 0.2b$. The Reynolds number is defined as $Re = U_0 b/\nu = 100$, where U_0 is the velocity of incoming flow and ν represents the kinematic viscosity. The mass ratio of structure and fluid equals to $m^* = \rho_s/\rho_f = 0.678$. The stiffness of the plate satisfies $E^* = E/\rho_f U_0^2 = 19\,054.9$, and the Poisson's ratio is $\nu_s = 0.4$.

A cubic region extending from $(-5b, -8b, -8b)$ to $(12b, 8b, 8b)$ is generated for the computational domain, as shown in Fig. 3(b). The
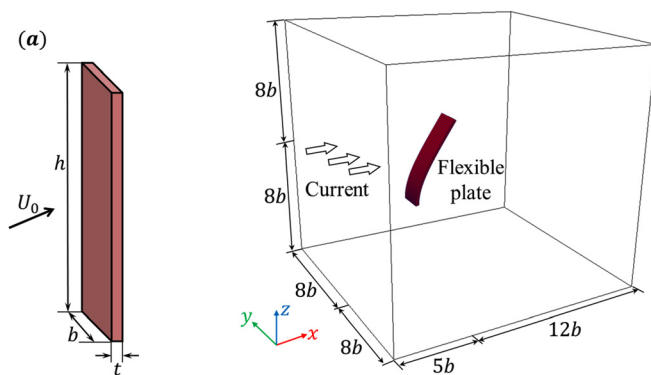
TABLE I. Plate deformation under different mesh resolutions.

No.	Grid number	d_{x}/b	d_{z}/b
Coase mesh	1.98	2.43	0.73
Medium mesh	3.14	2.38	0.70
Fine mesh	4.62	2.37	0.70

center of the plate locates initially at the origin of the computational domain. To better capture flow details around the elastic plate, a fine mesh with grid size of $0.02\,b(\Delta x) \times 0.02\,b(\Delta y) \times 0.04\,b(\Delta z)$ is adopted near the plate and in the near-field region. The total grid number is around 3.14×10^6. For the structure analysis, 1000 quadratic brick elements are adopted to model the flexible plate. No gravity and buoyancy are considered in the present numerical simulation.

2. Grid convergence test

To demonstrate the suitability of the aforementioned grid sizes, a grid convergence test is initially conducted. Three sets of grids with varying mesh resolutions are generated. The minimum grid sizes near the plate for the coarse, medium, and fine meshes are $0.04\,b$, $0.02\,b$, and $0.01\,b$, respectively. The same time step size of 2×10^{-4} s is employed for different mesh resolutions. A uniform current with Reynolds number of 100 is chosen for the test. The predicted platform deformations in different directions are presented in Table I. A comparison of the results reveals that the predictions obtained from the medium and fine meshes differ by less than 1%. Therefore, the numerical results under medium mesh are selected for subsequent analysis of flexible plate in a uniform current.

3. Plate deformation

Affected by the time-dependent hydrodynamic force, the flexible plate gradually deviates from the initial position and begins to bend and eventually reaches an equilibrium position, as shown in Fig. 4. The drag coefficient (C_D) of the plate at its equilibrium position is calculated as $C_{\mathrm{D}} = F_{\mathrm{x}}/(0.5\rho_f U_0^2 bh)$, where F_{x} is the total hydrodynamic force in the x-direction. The comparison with available numerical data is summarized in Table II. The discrepancy between the present
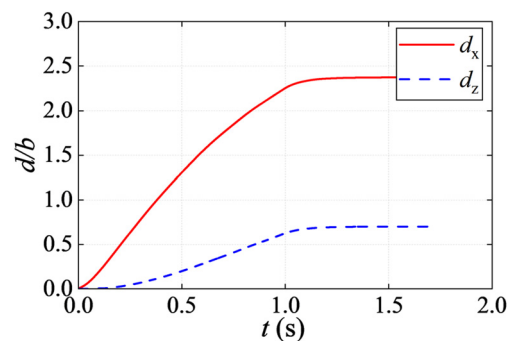

FIG. 3. Numerical set up for a 3D flexible plate in a uniform current: (a) geometry model and (b) computational domain.

FIG. 4. Time history of the deflection in the x- and z-directions of the center of the free end. d_{x} and d_{z} represent the deflection in the x- and z-directions of the center of the free end, respectively.

TABLE II. Summary of plate deformation and drag coefficient.

	C_D	d_x/b	d_z/b
Tian *et al.* (2014)	1.02	2.34	0.67
Luo *et al.* (2020c)	1.06	2.31	0.68
Present simulation	1.01	2.38	0.70

numerical simulation and the other published data is less than 5%, indicating a success of present tool for handling this FSI problem.

4. Flow field and plate stress

To better illustrate the FSI phenomena of this problem, we plot the pressure and velocity contour in Fig. 5. Due to the blockage effect, the pressure on the upstream side of plate is significantly greater than that on the downstream side. From the fixed end to the free end, the pressure on the upstream side gradually decreases, as well as the pressure difference between the upstream and downstream sides of plate. Moreover, the fluid velocity decreases rapidly after passing through the plate, especially in the downstream area of plate, where a significant low-speed zone exists, and a clear vortex is formed, as indicated by the streamlines. With the increase in distance, the downstream flow

velocity gradually recovers, and the vortex gradually dissipates. The stress distribution on the plate plotted in Fig. 6 reveals a gradually reduced stress from fixed end to free end. When observing across plate thickness, it is evident that the stress at the mid-layer of plate is significantly lower than that on its surface.

B. Case 2: Floating elastic disk in regular waves

This case study is selected from the wave basin experiments conducted by Montiel *et al.* (2013), which aims to validate a linear numerical model for predicting the flexural response of floating thin elastic disks. To ensure consistency between the experimental setup and the numerical model, the following requirements are applied: horizontal motions (surge, sway, and yaw) of the disk are restricted; linear motion is assumed; time-harmonic conditions are imposed; and the plate is assumed to be homogeneous.

1. Problem description

An elastic disk with a radius of 0.72 m and a thickness of 10 mm is selected for the analysis, as shown in Fig. 7(a). This disk is made of an expanded polyvinyl chloride (PVC) FOREX®, and the properties of the PVC are measured experimentally and summarized herein: the
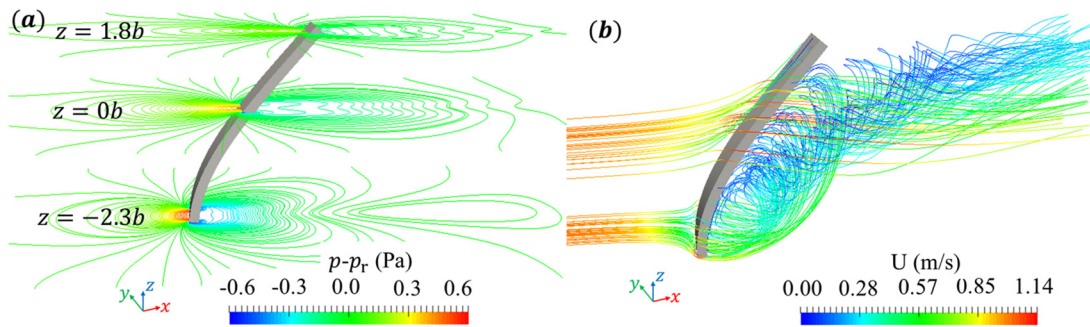

FIG. 5. Flow field of the flexible plate in a uniform current: (a) pressure contour on three representative horizontal planes, $p_r = 1 \times 10^4$ Pa represents the reference pressure at the center point of the computational domain and (b) streamlines colored by flow velocity.
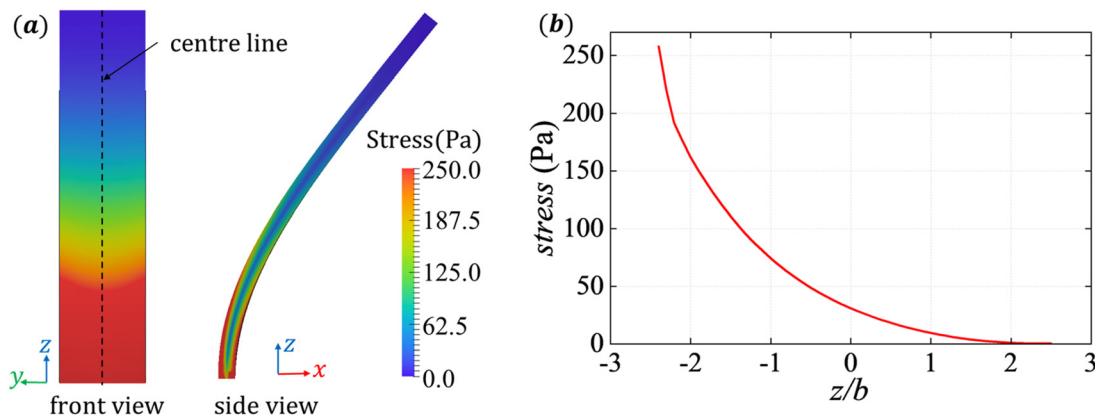

FIG. 6. Stress distribution: (a) on the surface of flexible plate and (b) along the centerline on the upstream surface of the flexible plate.
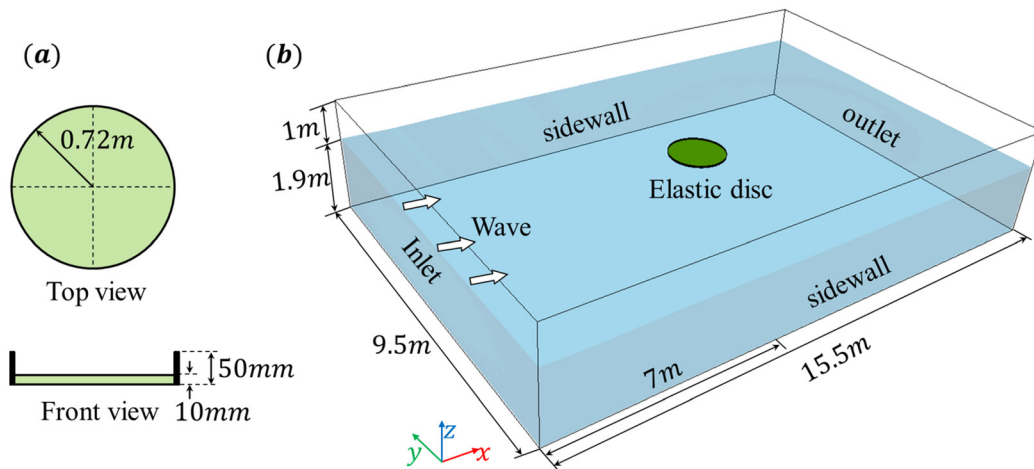
FIG. 7. Numerical setup for an elastic disk in regular waves: (a) geometry model of the elastic disk and (b) computational domain.

density is $530 \, \text{kg/m}^3$, and the Young's modulus and Poisson's ratio are 496 MPa and 0.3, respectively.

As shown in Fig. 7(b), a hexahedral region with dimensions of length 15.5 m, width 9.5 m and water depth 1.9 m is generated as the computational domain for our numerical simulations. The disk is placed at the center of the domain, with a draft of 5 mm. The distances from the disk to the inlet and sidewall are 7 and 4.75 m, respectively. To avoid the influence of the green water loads on the responses of the disk caused by flooding events, a barrier with a height of 50 mm is installed around the edge of the disk. To maintain consistency with the experimental conditions, the horizontal motion of the elastic disk is restricted, but it is free to move in the vertical direction. A small wave steepness of 1% and four different wave frequencies of 0.6, 0.8, 1.1, and 1.3 Hz are considered in the following simulations.

2. Mesh sensitivity study

To determine the appropriate grid size for the numerical simulation of the elastic disk in waves, a mesh sensitivity study is conducted. Three sets of grids are generated with varying mesh resolutions. For the coarse mesh, the minimum grid spacing on the disk is 0.04 m, while for the medium and fine meshes, this value decreases to 0.02

and 0.01 m, respectively. The total grid counts for the coarse, medium, and fine meshes are 0.81×10^6, 1.02×10^6, and 1.58×10^6. The incident wave used in the study has a frequency of 0.6 Hz and an amplitude of 44.6 mm. The time step is about $1.2 \times 10^{-3} \, T_w$ (wave period). Figure 8 illustrates the wave elevation and predicted displacement of the midpoint of the disk. It is observed that the wave elevation and displacement obtained using the medium and fine meshes are very close. As a result, the medium mesh with a time step of $1.2 \times 10^{-3} \, T_w$ is adopted for subsequent simulations.

3. Displacement of elastic disk

The predicted displacements in z-direction (d_z) at the center of the elastic disk are compared with experiment data, for both time-dependent curve and non-dimensional amplitudes (A_0) as shown in Fig. 9. It is seen that the time history of d_z shows reasonably good agreement with the experimental data, and the discrepancy of A_0 at different frequencies do not exceed 10%.

4. Wave-elastic disk interaction

To examine the impact of the disk on waves, we plot the wave surface elevation contours at 4 instants over one wave period, colored
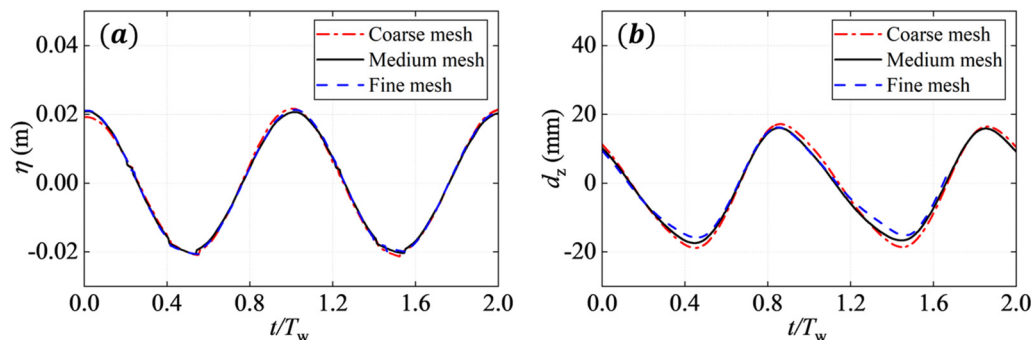

FIG. 8. Time history curves with different mesh resolutions: (a) wave elevation and (b) displacement of the midpoint of disk.
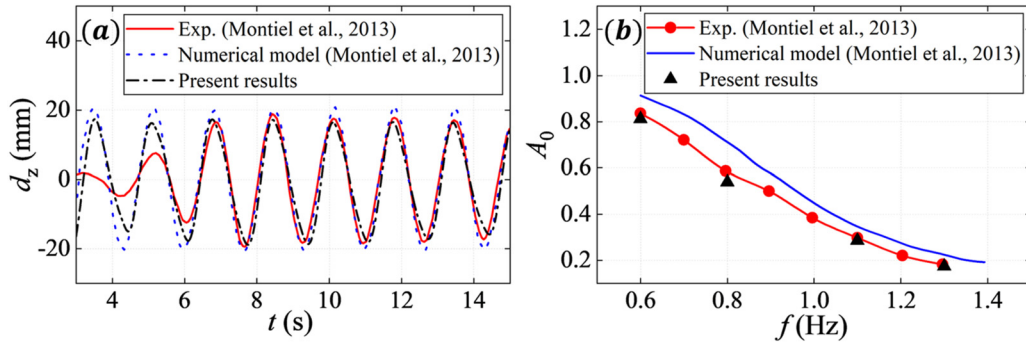
FIG. 9. Comparison of the displacement at the center of the elastic disk: (a) time history and (b) non-dimensional amplitude ($A_0 = A_d/A_w$, A_d is the amplitude of d_z).

by wave height in Fig. 10. Clearly, due to the presence of the disk, the incident wave exhibits obvious wave diffraction, with a significant decrease in wave amplitude and irregular changes in wave surface within the fan-shaped area behind the disk as indicated by the white solid lines. Additionally, the waveform in front of the disk also has irregular changes due to the radiated waves caused by the heave motion of the elastic disk. Moreover, the wave surface on the bottom surface of the disk at different instants is shown in the upper left corner of Fig. 10. Because of the shallow draft, air is entrained into the bottom of the disk during the interaction

between the incident wave and the disk, resulting in a significant pressure reduction on the bottom surface of the disk, as shown in Fig. 11, which further leads to a non-uniform bending deformation, as shown in Fig. 12.

C. Case 3: Flexible OWC WEC in regular waves

In this section, the Poly-A-OWC model, studied experimentally in wave tank and analytically by Moretti et al. (2019), is chosen for the analysis of flexible OWC WEC.
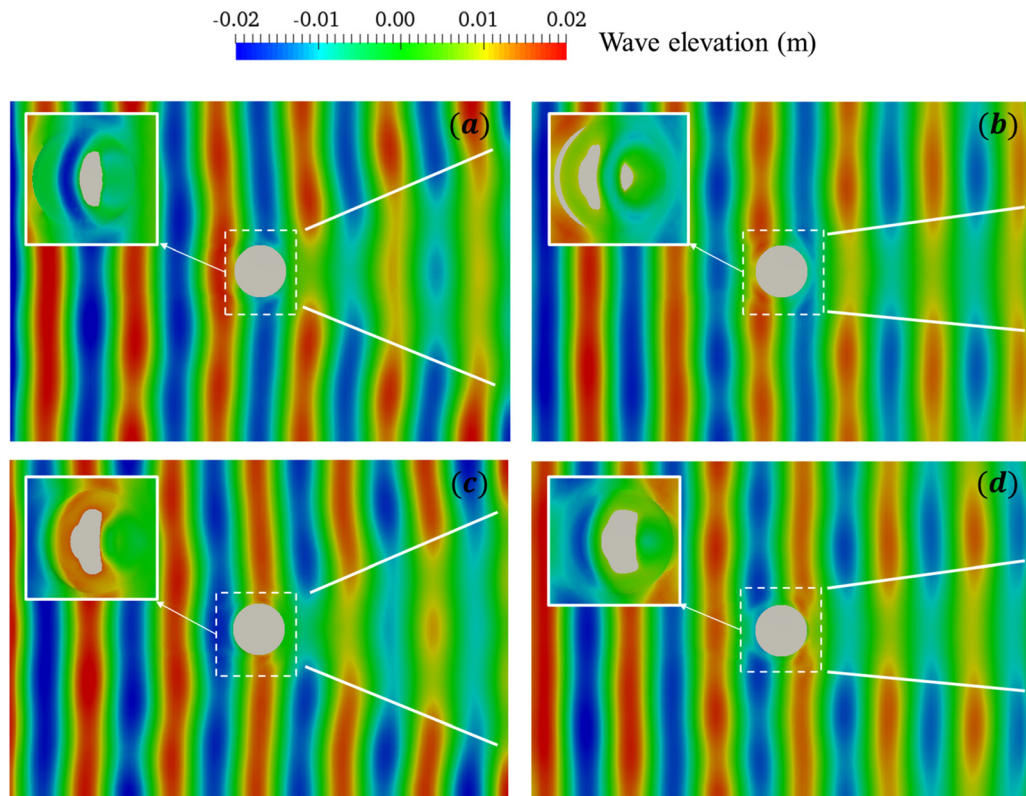

FIG. 10. Wave surface elevation at 4 instants over one wave period (the wave surface at the bottom of the elastic disk is displayed in the left upper corner): (a) $t = 0.1\ T_w$; (b) $t = 0.35\ T_w$; (c) $t = 0.6\ T_w$; and (d) $t = 0.85\ T_w$.
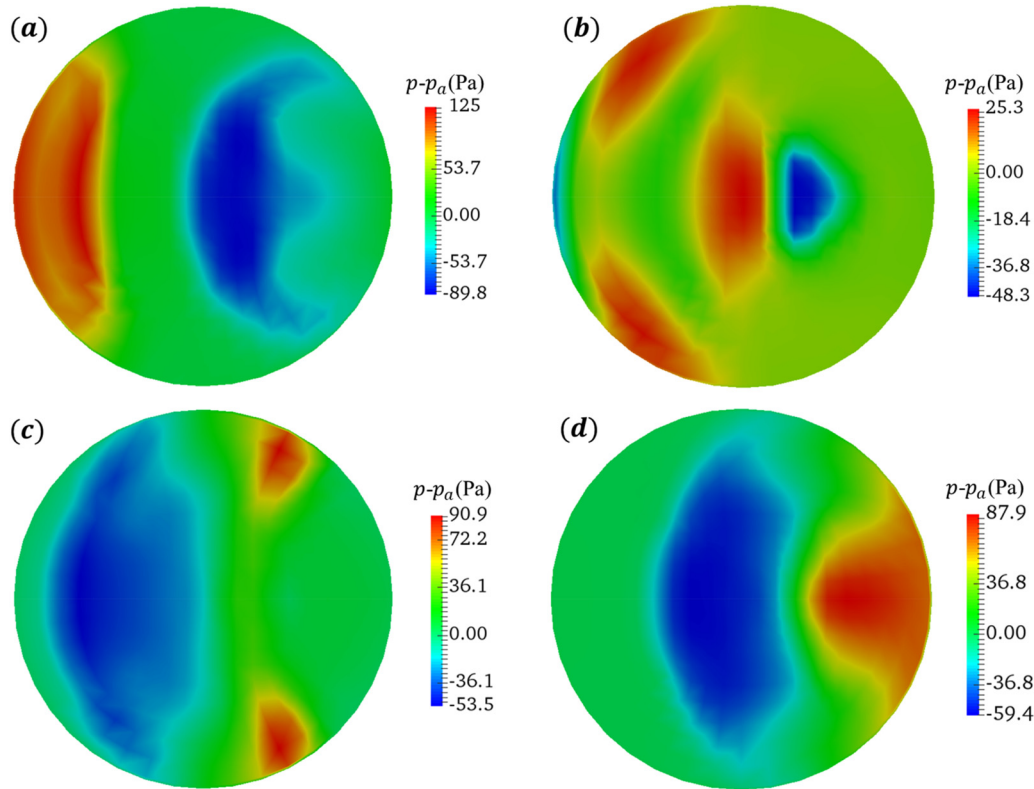
FIG. 11. Pressure distribution on the bottom surface of the elastic disk at 4 instants over one wave period, where p_a represents the standard atmospheric pressure: (a) $t = 0.1\,T_w$; (b) $t = 0.35\,T_w$; (c) $t = 0.6\,T_w$; and (d) $t = 0.85\,T_w$.

1. Poly-A-OWC model

Poly-A-OWC model consists of an axial-symmetric U-shaped collector and a circular diaphragm dielectric elastomer generator (CD-DEG) located at its top. In this design, CD-DEG replaces the traditional mechanical PTO, which shows its advantages of simple structure, low cost and high density of converted energy per unit mass (Falnes, 2004). In our CFD simulations, the CD-DEG PTO is modeled as a flexible membrane, and the electric field of the PTO is ignored. More details about the Poly-A-OWC model can found in the study by Moretti *et al.* (2019).

The computational domain, displayed in Fig. 13(a), has a water depth of 2 m, a width of 2 m, and a length of 5 m. The Poly-A-OWC model is placed in the center of the computational domain. The top of the OWC collector is covered with a flexible membrane with a diameter of $d_m = 400$ mm and a thickness of 2 mm, which is made of acrylic VHB 4905. The density and Poisson's ratio of the membrane are 960 kg/m^3 and 0.49, respectively. A hyper-elastic Mooney–Rivlin model (Mooney, 1940; Rivlin, 1948) defined by a strain energy potential equation [Eq. (14)] is used to describe the mechanical properties of the material,

$$W = C_{10}(\bar{I}_1 - 3) + C_{01}(\bar{I}_2 - 3), \tag{14}$$

where $\bar{I}_1$ and $\bar{I}_2$ are the first and the second invariant of the left Cauchy–Green deformation tensor, respectively, C_{10} and C_{01} are

empirically determined by material constants, which are set to 5500 and 570 Pa (Moretti *et al.*, 2019). The nonlinear stress-strain behavior of the flexible material is shown in Fig. 13(b).

It is noted that a large pre-stretch (λ_p) of 3.5 is applied to the flexible membrane in the experiment, meaning that the membrane is uniformly pre-stretched to a diameter $d_m = \lambda_p d_0$ (where the initial diameter $d_0 = 114$ mm) (Moretti *et al.*, 2019). In our simulation, we set $\lambda_p = 1$ and $d_0 = 400$ mm to ensure numerical stability in the modeling.

2. Mesh sensitivity study

In order to determine the optimal grid size for simulating the Poly-A-OWC WEC in regular waves, a mesh sensitivity analysis is first performed. Three sets of grids with different mesh resolutions are adopted for the test. The minimum grid spacing on the flexible membrane is set at 6, 4, and 2 mm for the coarse, medium, and fine meshes, respectively. The total number of grids for each mesh category is 1.11 $\times$ 10^6, 1.61 $\times$ 10^6, and 2.27 $\times$ 10^6, respectively. The incident wave used in the test has a frequency of 0.5 Hz and an amplitude of 0.05 m. To accurately capture the wave dynamics, a time step of 1.0×10^{-3} T_w (wave period) is selected. The time history of the generated wave elevation and predicted displacement of the membrane's midpoint is presented in Fig. 14. Upon comparison, it is observed that the medium resolution setup adequately captures the deformation of the flexible
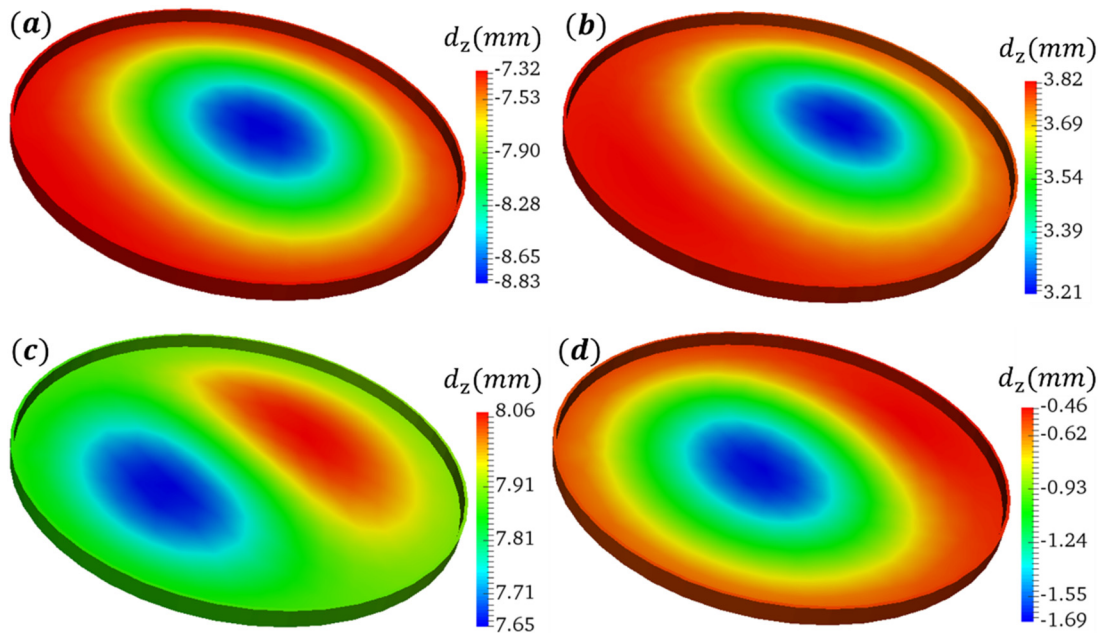
FIG. 12. Deformation of the elastic disk in z direction at 4 instants over one wave period: (a) $t = 0.1\ T_w$; (b) $t = 0.35\ T_w$; (c) $t = 0.6\ T_w$; and (d) $t = 0.85\ T_w$.

membrane. Hence, the medium grid, along with a time step of $1.0 \times 10^{-3}\ T_w$, is selected for subsequent simulations.

3. Resonant responses

According to the study of Moretti *et al.* (2019), the Poly-A-OWC model has a resonant frequency of $f_r = 0.4\ Hz$ when only the OWC collector is considered, and the adding of the flexible membrane increases the system's f_r to $0.5\ Hz$. To capture this resonance, we consider a range of wave frequencies, which are summarized in Table III.

In addition, two scenarios are considered: (a) the collector only and (b) the collector and the membrane.

In addition to the CFD-FEA analysis tool, we also used Wave Venture TE^{TM} (Wave Venture Ltd., 2023) to simulate the Poly-A-OWC model. The comparison among these three is shown in Fig. 15. For scenario (a), the calculated response amplitude operator (RAO) shows fairly good agreement with both the experimental data and Wave Venture TE^{TM}. However, when the flexible membrane is included in scenario (b), discrepancies between the CFD and experimental results are observed. This discrepancy can be attributed to the
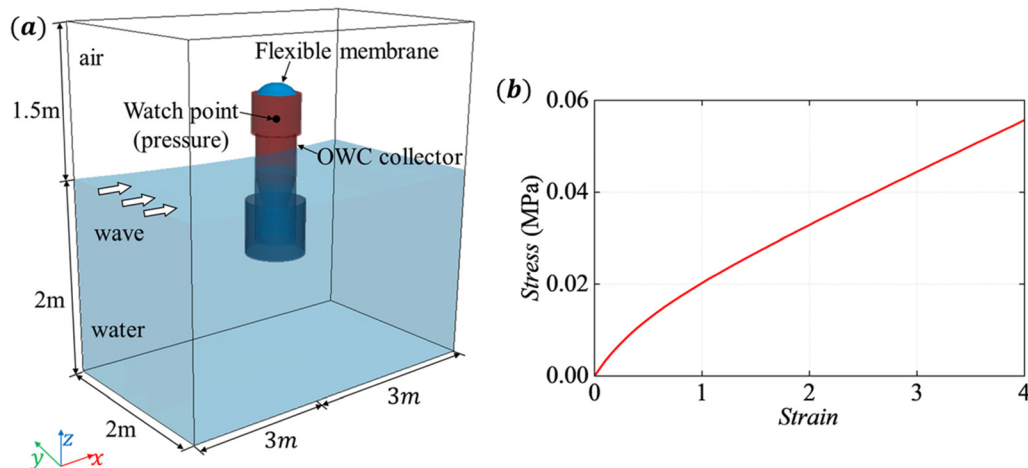

FIG. 13. (a) Computational domain of numerical simulation and (b) strain–stress curve of the flexible material.
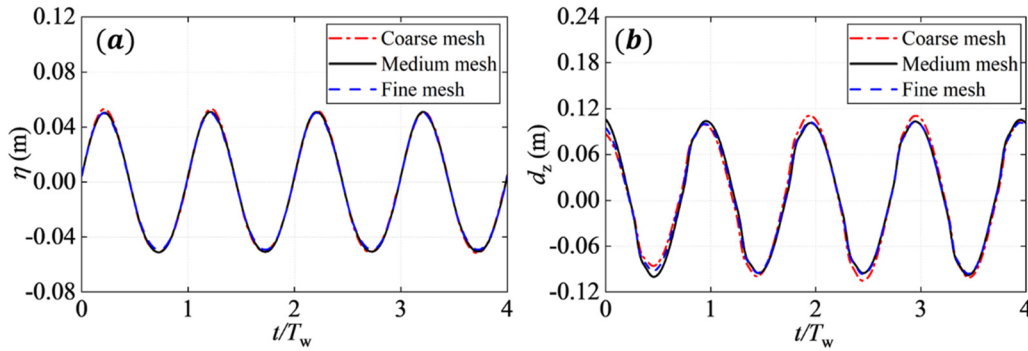
FIG. 14. Time history curves with different mesh resolutions: (a) wave elevation and (b) displacement of the midpoint of membrane.

TABLE III. Summary of wave conditions.

Wave frequency f_w	Wave amplitude A_w	Wavelength λ_w
0.2–0.7 Hz	0.05 m	3.2–21.0 m

absence of pre-stretching of the flexible membrane in the CFD modeling. Currently, the code can only handle pre-stretch up to 5% due to numerical instability, while the pre-stretch is as high as 350% in the experiment. The results also suggest that pre-stretch increases the natural frequency of the system, as indicated by the higher measured resonant frequency compared to the predicted value by the present CFD tool [Fig. 15(b)]. It is worth noting that the CFD results are close to those of Wave Venture TE^{TM} when $\lambda_p = 1$, and Wave Venture TE^{TM} results are consistent with the experiment data when $\lambda_p = 3.5$, which indicates that our numerical simulation results are reasonable.

4. Flow field and membrane stress

To better understand the FSI response of the Poly-A-OWC model in waves, we plot the wave surface and streamlines in the air chamber at 4 instants within one wave period, as shown in Fig. 16. In addition, time-history curves of other variables, such as the wave height inside OWC collector (η), pressure at the watch point (p_A), and

deformation of the flexible membrane (d_z), are displayed in Fig. 17. When the incident waves cause the water elevation in the OWC collector to rise, the pressure inside the air chamber increases, causing the membrane to deform outward. Conversely, the membrane deforms inward when the water level decreases. This phenomenon is consistent with the instantaneous plots in Fig. 17, reflecting a synchronized variation of η, p_A, and d_z.

Furthermore, we estimate the generated power of the Poly-A-OWC model (P_w) using the power of the water column in the OWC collector acting on the flexible membrane, which is defined by the following equation:

$$P_w = \bar{p} S \dot{\eta}, \quad (15)$$

where S denotes the cross-sectional area of OWC collector, $\dot{\eta}$ represents the moving velocity of the water column, $\bar{p}$ is the space-averaged pressure above water surface in the collector. As indicated by Fig. 16, the pressure distribution in the air chamber is almost uniform, thus the pressure at the watch point is used for the calculation of P_w. As shown in Fig. 18, P_w periodically varies over time, with a time-averaged value close to 0, indicating that almost no energy generates. This is due to the absence of the electric field in the simulation for CD-DEG. If included, the elastic potential energy stored in the flexible membrane can be partially converted into electrical power instead of being entirely dissipated in the flow field.
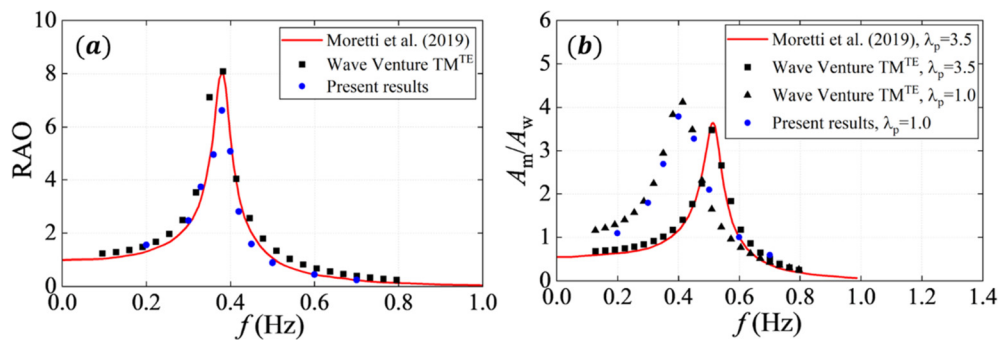

FIG. 15. Comparison of numerical results and experiment data: (a) collector only and (b) collector and flexible membrane, where A_m is the displacement amplitude of the midpoint of membrane in the z-direction.
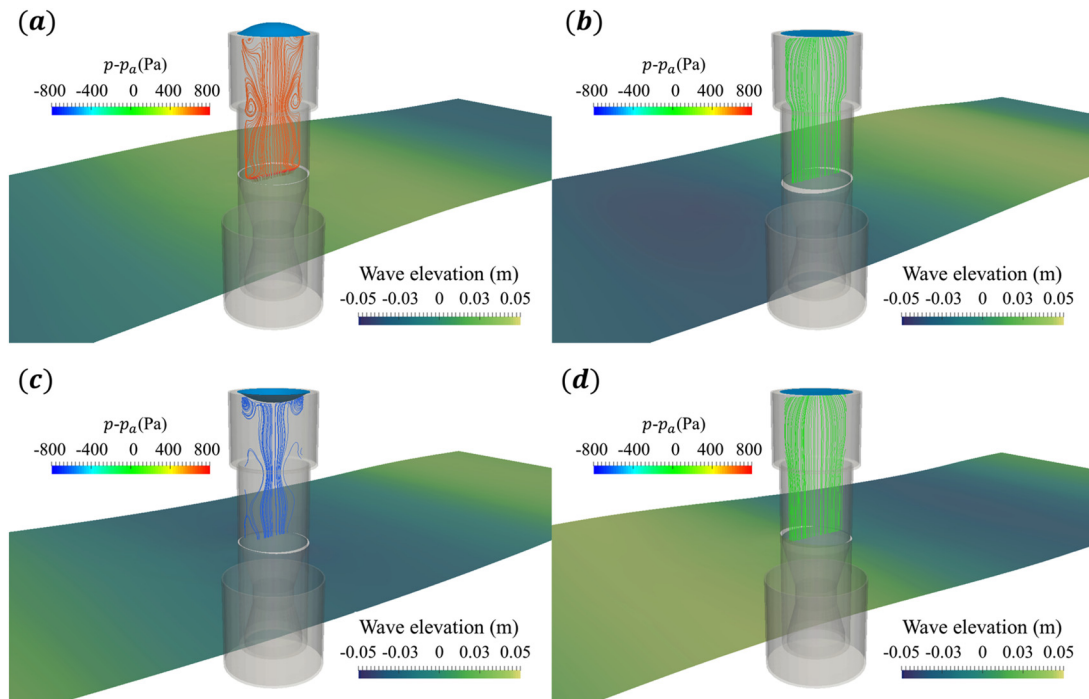
31 August 2023 11:33:34

FIG. 16. Wave surface (colored by wave elevation) and streamlines in the air chamber (colored by pressure) at 4 instants within one wave period, where p_a is the standard atmospheric pressure: (a) $t = 0.1\,T_w$; (b) $t = 0.35\,T_w$; (c) $t = 0.6\,T_w$; and (d) $t = 0.85\,T_w$.

In addition, Fig. 19 shows the stress-strain distribution of the membrane when it is deformed to the maximum point. The strains at the middle and edge areas are greater than that at other locations, indicating a thinner thickness and higher risk of structure failure in those areas, therefore reinforcing the structure should be considered to minimize the risk of potential failure. In addition, the uneven distribution of membrane thickness has an adverse effect on the power generation efficiency of CD-DEG.

D. Case 4: Flexible tube WEC in regular waves

A distensible tube wave energy converter namely Anaconda (Farley and Rainey, 2011) is chosen for the analysis of the flexible tube

WEC in waves. Compared with Poly-A-OWC model, the Anaconda model requires an external and internal flow coupling by a distensible tube, resulting in a high challenge FSI dynamic modeling.

1. Anaconda model

As shown in Fig. 20, we simulate the Anaconda WEC, which is taken from the study of Mendes et al. (2017). The model consists of wood bow, flexible rubber tube and stern, whose material properties are summarized in Table IV. The tube has a length of $L = 2.44$ m and initial radius of $R_0 = 0.077\,15$ m. The tube thickness is $h_0 = 2$ mm. In the experiment, the tube bow is free to move, while the stern is fixed.
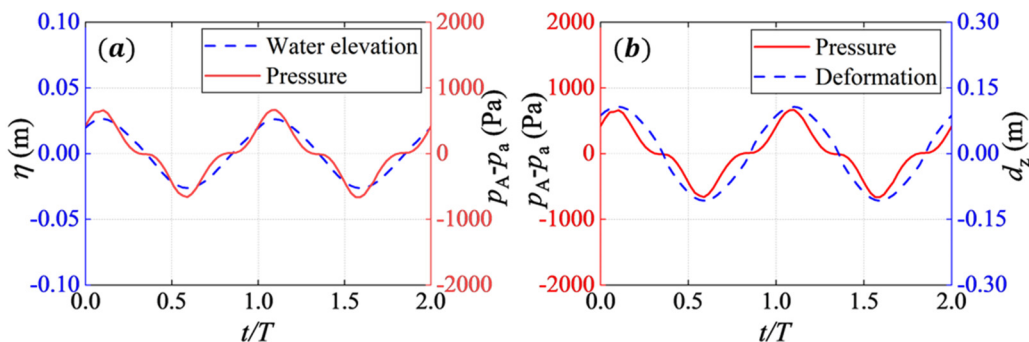

FIG. 17. Time-history of variables: (a) wave elevation (η) in the OWC collector and pressure at the watch point and (b) pressure at the watch point and displacement of the midpoint of the flexible membrane (d_z) in the z-direction, where p_a denotes the standard atmospheric pressure.
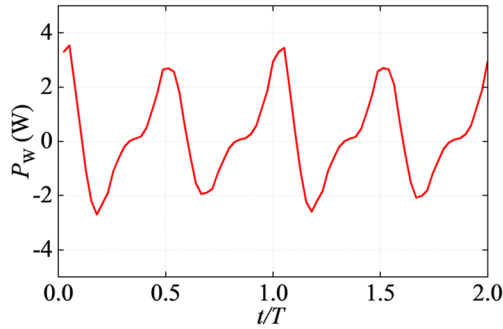
FIG. 18. Time history of the estimated power of the Poly-A-OWC model.

To consider the impedance of the WEC power-takeoff, an orifice plate is placed on top of vertical tube. In our simulation, the orifice plate is replaced and modeled by a porous media setting in OpenFOAM, which can provide adjustable impedances.

TABLE IV. Summary of material properties.

Material	Density (kg/m³)	Young's modulus (MPa)	Poisson's ratio
Rubber	960	0.91	0.5
Wood	700	8100	0.3
Stainless steel	7850	2.1×10^5	0.3

2. Porous media model

In OpenFOAM, the porous media is modeled by adding a source term (f_s) to the Navier–Stokes equations [Eq. (2)], where f_s is the source term induced by the porous media, defined by Darcy–Forchheimer equation (Barree and Conway, 2004),

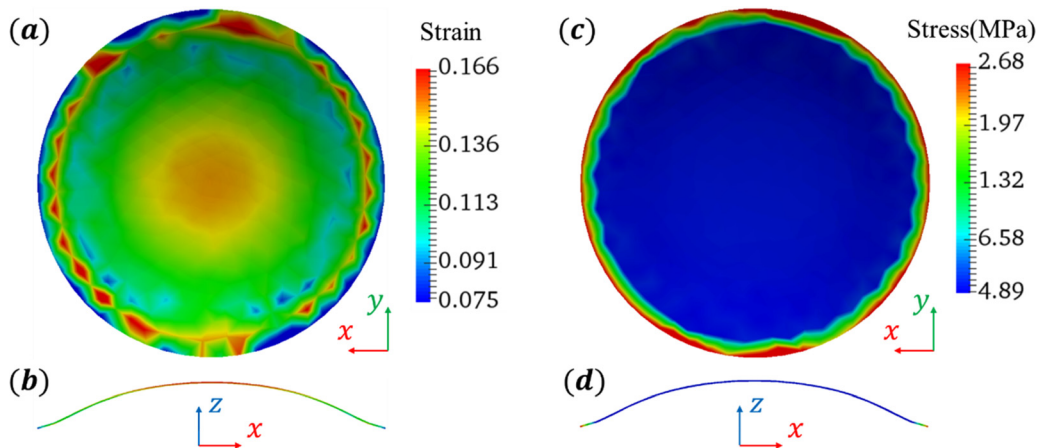$$f_s = -\left(\mu D + \frac{1}{2}\rho|U|F\right)U, \tag{16}$$

FIG. 19. Structural responses of the flexible membrane when the deformation reaches the maximum (a) strain distribution on the bottom surface of the membrane; (b) strain distribution on the cross section; (c) stress distribution on the bottom surface of the membrane; and (d) stress distribution on the cross section.
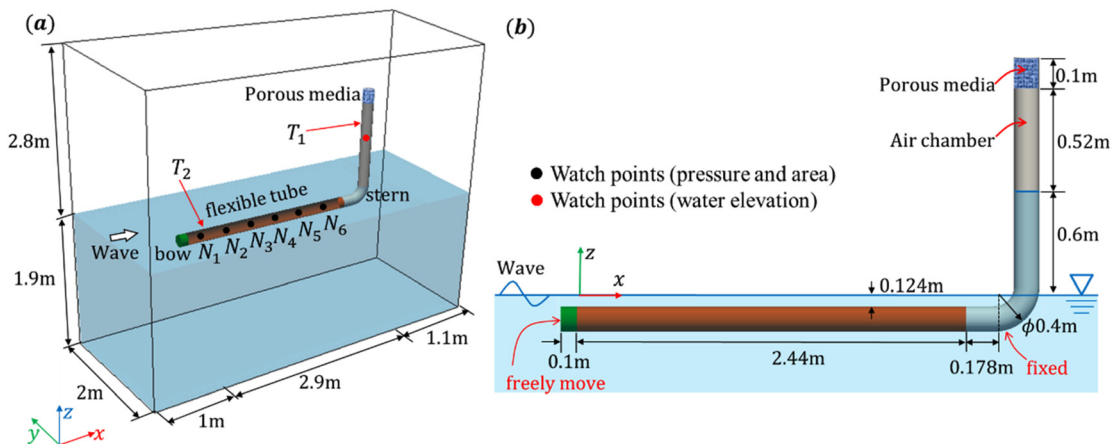

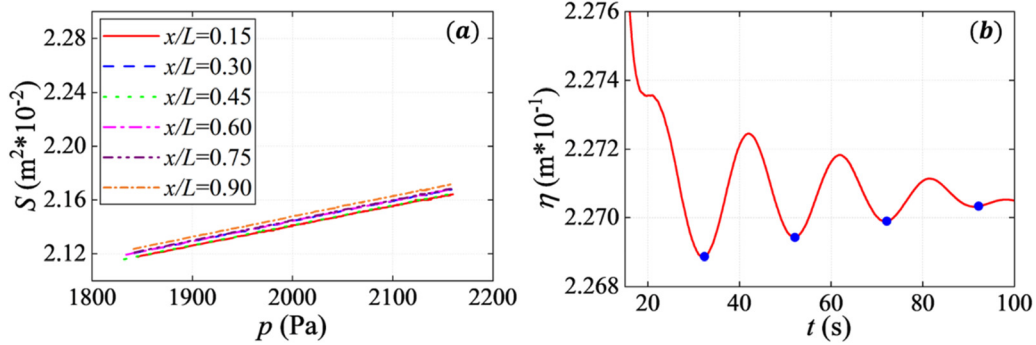**FIG. 20.** Schematic diagram of Anaconda WEC model: (a) computational domain and (b) geometric dimensions.

FIG. 21. (a) Tube cross-sectional area-pressure relation along T2 and (b) water surface in T1 (blue points represent the local minima).

TABLE V. Summary of wave conditions.

Wave frequency f_w	Wave speed C_g	Wave amplitude A_w	Wavelength λ_w
0.2–0.5 Hz	3.01–4.10 m/s	0.05 m	6–20.5 m

f_s is composed of a viscous loss and an inertial loss, which are proportional to the velocity and the square of velocity, respectively. D and F are coefficients, determined by physical properties of the porous media material. More detailed information about this model and its implementation can be referred to Lachaud and Mansour (2014). In this work, a simple homogeneous porous media with linear damping is selected; therefore, $F = 0$. In addition, D is set as 2×10^{10} to provide significantly large impedance.

3. Free decay test

A free-decay test is conducted first to determine the natural frequency of OWC in vertical rigid tube (T1) and bulge wave speed in horizontal flexible tube (T2), as shown in Fig. 20(a). An initial water column with a height of 0.6 m in T1 is allowed to flow into the flexible tube (T2) with an initial radius of $R_0 = 0.07715$ m, causing tube's contraction and expansion with time before the water level in T1 finally

approaches a constant as 0.227 m. After reaching the steady state, the radius of T2 increases to $r_0 = 0.0827$ m. The recorded pressure-tube-cross-sectional area variations (N_1 to N_6) and water elevation in T1 are shown in Figs. 21(a) and 21(b). With Fig. 21(b), the oscillatory period of OWC is calculated as 18 s, and thus, the natural frequency of this OWC is 0.056 Hz.

According to the linear theory described in Lighthill (2001), the bulge wave speed (C_b) of a homogeneous tube can be determined by water density ρ_1 and the distensibility D_t, namely,

$$C_b = 1/\sqrt{\rho_1 D_t} \quad \text{and} \quad D_t = \frac{1}{S}\frac{\partial S}{\partial p}, \tag{17}$$

where S is the cross-sectional area and p is the pressure difference across the tube wall. With Eq. (17) and Fig. 21(a), the estimated bulge wave speed C_{b1} is 3.77 m/s for a water density of 1025 kg/m³. The above linear theory was extended by Chaplin et al. (2012) to consider the distensibility of inhomogeneous tube covered with inextensible fibers,

$$D_t = \frac{3R_0}{2Eh_0}\frac{r'(r'-1+\alpha)^2}{\alpha-(r'-1)^2}, \tag{18}$$

where, R_0, h_0, α, E, and r' are the radius of unstressed tube, wall thickness, the proportion of uncovered rubber in the total circumferential of the undeformed rubber tube, Young's modulus, and ratio of the radius of the tube before and after deformation.
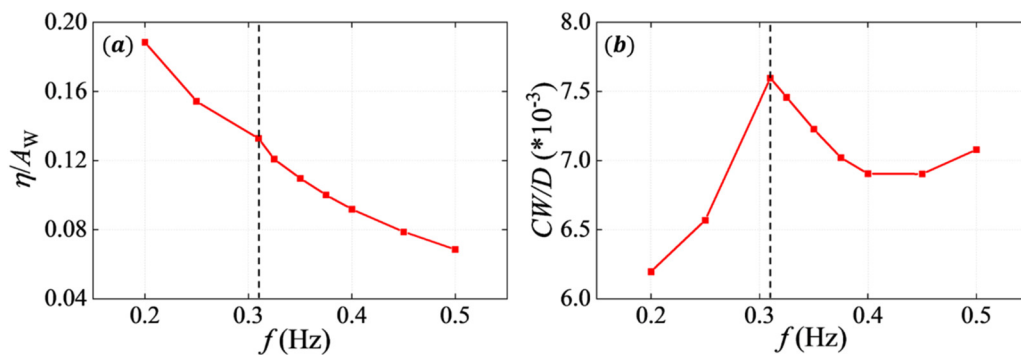

FIG. 22. Responses of Anaconda WEC under a series of wave frequencies: (a) OWC surface elevation in T1, normalized by wave amplitude and (b) capture width, normalized by the tube diameter.
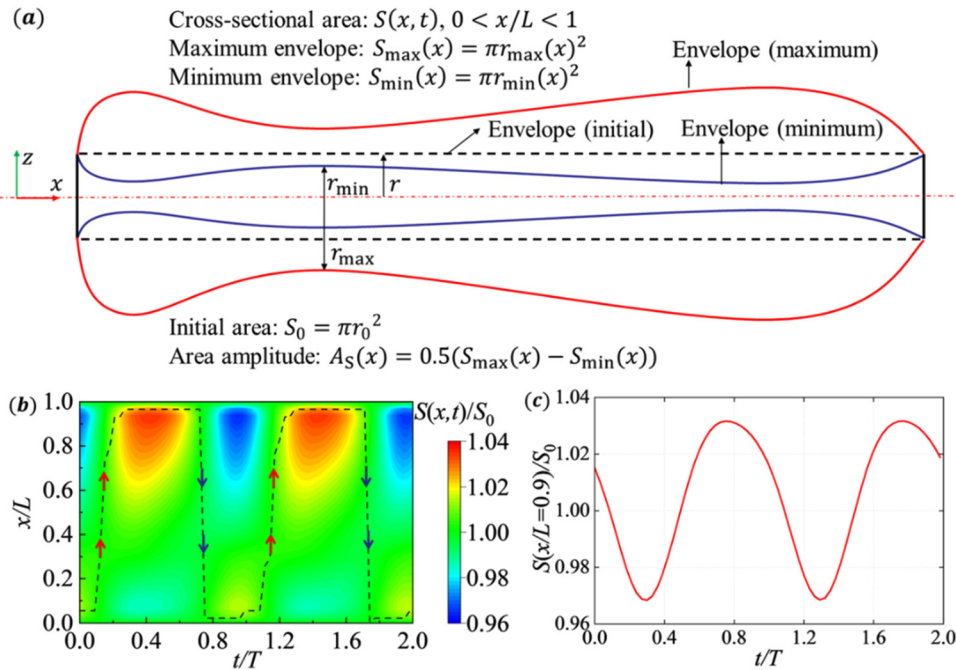
FIG. 23. Predicted bulge waves along T2 at $f_w = 0.31$ Hz: (a) definition of variables. The red and blue lines represent the envelopes for $S_{max}(x)$ and $S_{min}(x)$, respectively; (b) time and spatial distribution of cross-sectional area (normalized by initial area, $T = 3.23$ s is the wave period); and (c) time history of cross-sectional area at $x/L = 0.9$ (normalize by initial area).

The bulge wave speed obtained from Eq. (18) is $C_{b2} = 3.45$ m/s. The discrepancy between C_{b1} and C_{b2} is 9%, which is within an acceptable range as pointed out by Pedley (1980) for any "fluid mechanical and elastic nonlinearities" phenomena study.

4. Resonant responses

The studies conducted by Chaplin *et al.* (2012) and Farley *et al.* (2012) suggested that the resonance phenomenon of the Anaconda WEC occurs when the external water wave speed matches the tube internal bulge wave speed. To verify this, we consider a range of wave speeds, summarized in Table V. Given that $C_{b1} = 3.77$ m/s for the current setup, we expect to observe the resonant phenomena when external wave speed C_g equals to C_{b1}. According to Stokes wave theory (Toland, 1996), the wave frequency corresponding to a wave velocity of 3.77 m/s at a water depth of 1.9 m is 0.31 Hz.

Figures 22(a) and 22(b) display our CFD results for OWC water surface elevation (η) in T1 and capture width of Anaconda WEC, respectively. The generated power (W_e) and capture width (CW) are defined as

$$W_e = \int_0^{T_w} p(t)Q(t)\mathrm{d}t \quad \text{and} \quad CW = \frac{W_e}{\frac{1}{2}\rho g A_w^2 C_g}, \quad (19)$$

where p and Q are the space-averaged pressure in the air chamber below the porous media and volume flux across the porous media, respectively. It is seen that a peak value of CW/D is very well captured at $f_w = 0.31$ Hz, and a jump in η/A_w is also observed at $f_w = 0.31$ Hz, indicating the resonant response of Anaconda WEC is accurately captured.

It is known that one specific feature of Anaconda WEC is the bulge wave along flexible tube. Under the resonant condition, the tube cross-sectional area ($S(x,t)$) gradually increases along the tube (Chaplin *et al.*, 2012). To verify this finding, we plot the predicted time and spatial distribution of $S(x,t)$ at $f_w = 0.31$ Hz in Figs. 23(a)–23(c).

The periodical variation of $S(x,t)$ is observed in Fig. 23(b), and the time history of S at $x/L = 0.9$ plotted in Fig. 23(c) provides a more intuitive illustration, implying that bulges generate in the flexible tube. To indicate the bulge wave's propagation along the tube, we construct a dashed line consisting of $S_{max}(x)$ representing the bulges at different instants in Fig. 23(b). The forward- (red arrows) and backward-traveling (blue arrows) bulge waves are observed. Moreover, $S_{max}(x)$ reaches its maximum value at the tube end, which is consistent with the findings of Chaplin *et al.* (2012).
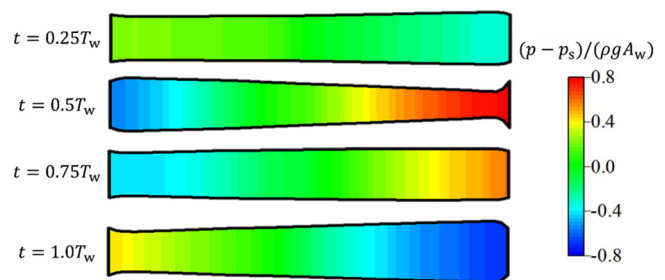

FIG. 24. Pressure contour (normalized by $\rho g A_w$, and $p_s = 2023$ Pa is the hydrostatic pressure along the central line of the tube) at tube central plane at 4 instants over one wave period. Solid boundary lines represent the deformed shape of the flexible tube.
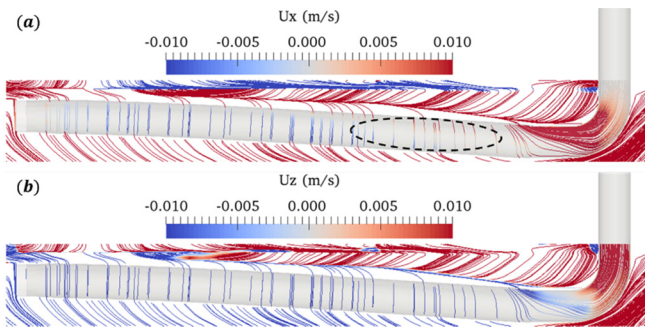
FIG. 25. Instantaneous streamline in the central plane colored by flow velocity: (a) U_x and (b) U_z.

FIG. 27. Instantaneous structural responses of the flexible tube: (a) strain and (b) stress.

Obviously, the generation of bulges is closely related to the pressure distribution in the flexible tube. The predicted pressure contours at the central plane of the tube, at 4 instants over one wave period, are displayed in Fig. 24. The forward- and backward-traveling bulge waves can also be observed. Here, the pressure distribution at a given tube cross-section is almost the same (Huang *et al.*, 2023).

The advantage of using high-fidelity CFD-FEA modeling for this problem is that it can provide detailed and accurate fluid and pressure field information, such as the streamline plots in Fig. 25, in which reversed fluid flow can be clearly captured, as indicated in the circle. A reduced order model with one-dimensional assumption is unable to deal with this. In addition, under some wave conditions, the WEC tube may float above water surface and break incident wave, thus generates nonlinear waves, as shown in Fig. 26 from our CFD simulation. However, it is entirely ignored in the reduced order model. Moreover, a CFD-FEA tool can provide comprehensive structural deformation characteristics, such as stress and strain distributions, to ensure the device's reliability or optimize it under diverse operating conditions for the design of WECs. As indicated in Fig. 27, the stress in the vicinity of tube end is significantly larger than the rest parts of tube. Therefore, reinforcement treatment is recommended to avoid potential structural failure.

IV. DISCUSSIONS AND CONCLUSIONS

In this work, we establish a numerical analysis tool based on CFD-FEA method to simulate the FSI problem of fWECs in waves. Within this framework, the fluid flow around fWEC is predicted by solving the three-dimensional unsteady Navier–Stokes equations with finite volume approach. The structure deformation is obtained by using a finite element method to solve the momentum
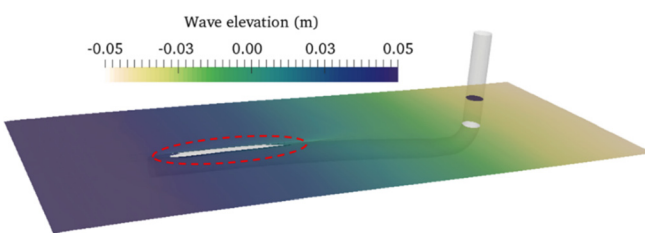

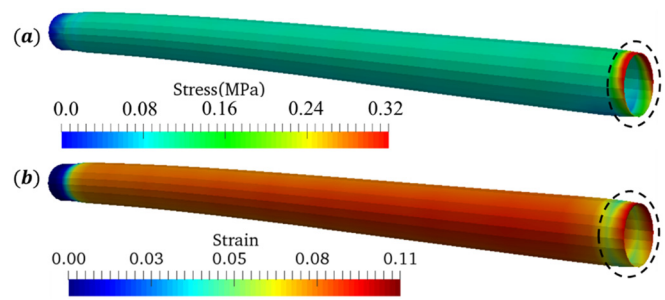**FIG. 26.** Instantaneous wave surface colored by wave elevation.

balance equations in a weak form. A strong coupling strategy with an IQN-ILS algorithm is utilized to enhance the numerical stability and convergence of the iterative process. This tool is successfully applied to several FSI problems as demonstrated by our case studies. From the results presented above, in this section, we discuss the performance of the present FSI analysis tool for simulating fWECs, focusing on its convergence, computational cost, capabilities, and limitations.

A. Convergence

It is generally accepted that it is hard to reach a convergent solution for the study of wave-flexible-structure interaction problem, as it requires a simultaneous convergence of fluid, structure, and coupling calculation. For a fWEC modeling, the air–water free surface induced by the incident wave further increases the challenges of FSI simulation. Although finer meshes, smaller time steps, and tighter convergence constraints, given by Eq. (13), can improve the convergence, they require more computational resources. To avoid the breakdown of the solution, which can be caused by setting up the initial fields that are far away from final solutions, a ramp scheme is a good choice for the force mapping from fluid field to solid structure field. In addition, coupling strategies between structure and fluid solvers have significant impacts on the solution's convergence and computational time, among which the acceleration scheme is one example (Mehl *et al.*, 2016; Haelterman *et al.*, 2016; and Huang *et al.*, 2023).

B. Computational cost

In this study, all numerical simulations are performed using the Cirrus UK National Tier-2 HPC Service at EPCC. Cirrus standard compute nodes each contain two 2.1 GHz, 18-core Intel Xeon E5–2695 (Broadwell) series processors. The computational cost for different case studies is presented in Table VI in which T_w represents the wave period.

It is worth noting that the convergence of FSI coupling simulation varies for different physical problems. This means that the number of sub-iteration steps required to achieve convergence within a time step may differ. Consequently, even when utilizing the same grid, time step, and simulation time, the overall computation time may vary across different problem scenarios. A typical example is case 4, where, despite having fewer grid number and a shorter simulation time compared to case 3, it requires a longer computation time.

TABLE VI. Computational cost of different case studies.

No.	Grid number	Time step	Simulation time	CPU number	Clock time
Case 1	3.14×10^6	2×10^{-4} s	1.7 s	108	29.1 h
Case 2	1.02×10^6	$1.2 \times 10^{-3} T_w$	$12 T_w$	108	41.4 h
Case 3	1.61×10^6	$1.0 \times 10^{-3} T_w$	$15 T_w$	108	52.1 h
Case 4	1.06×10^6	$1.0 \times 10^{-3} T_w$	$10 T_w$	108	61.6 h

C. Capabilities

The present analysis tool has been successfully applied to the analysis of two different types of fWECs, i.e., Poly-A-OWC and Anaconda, taking into account the nonlinear stress-strain behavior of hyper-elastic material, the effects of six-degree-of-freedom (6DoF) motions, and the impedance of PTO modeled by a porous media model. With the results presented above, we have demonstrated the tool's accuracy through comparisons with other numerical results and experimental data. We can conclude that the FSI analysis tool can provide rich flow field information and structural response details, such as the flow field velocity, pressure, and structural stress distribution. More importantly, this tool is capable of capturing unsteady flows and nonlinear phenomena, such as the development of vortex wake behind the deformed flexible plate [Fig. 5(b)], irregular variations of wave surface (Fig. 10), non-uniform bending deformation of the elastic disk (Fig. 12), non-uniform strain distribution of the deformed membrane on the top of Poly-A-OWC WEC (Fig. 19) and the bidirectional fluid flow across the cross section of Anaconda WEC (Fig. 25), which is unable to deal with using reduced-order models. The detailed information provided by the FSI analysis tool is helpful for gaining a deep understanding of the physical mechanism of fWEC devices and for enhancing their design. In addition, the tool is able to handle 6DoF motions and mooring lines, which is important for fWEC's analysis.

D. Limitations

The limitations of the present tool are mainly in the following areas: (a) Compared to reduced ordered models, this tool requires much more computational resources, making it unsuitable at the initial design stage of fWECs, where a large number of simulations are needed to determine the proper device geometric and hydrodynamic parameters. (b) At present, the tool cannot handle a large pre-stretch of flexible materials, less than 5%. Indeed, in most experimental testing, the materials are subjected to a large pre-stretch deformation over 100% to prevent negative stresses and reduce the risk of structural failure (Vertechy et al., 2013; Moretti et al., 2019). However, this imposes significant instability issue in our simulations (Li et al., 2011; Jiang et al., 2016). (c) Past studies indicated that, for fWECs using direct PTO with DEG material, the material deformation is also linked to the electric field imposed on material (Vertechy et al., 2013; Rosati Papini et al., 2018). However, the present tool is limited to fluid-structure couple excluding the electric field. This will be covered in our near future study. (d) Due to the limitations in moving mesh handling techniques, this tool has limitations to handle large structure's deformation, which may exist under extreme wave conditions. (e) The experimental studies suggest that flexible materials used in fWECs, such as silicone, acrylic, polyurethanes, and natural rubbers, etc., are typically viscoelastic materials (Liao et al., 2020; Collins et al., 2023). Therefore, viscoelastic models are required to obtain more accurate results. However, these models are not available in the present tool.

Nevertheless, the present work provides a powerful numerical analysis tool for simulating the FSI phenomena of fWECs in waves and contributes to exploring the complex FSI dynamic response of fWECs. It is worthwhile to mention that the tool is not limited to homogeneous materials, instead, it can handle flexible materials with multi-layer structure or non-uniform stiffness distribution. Further applications can be extended to the FSI studies on the passive deformation of flexible structures with complex materials, such as hydro-elastic responses of floating offshore wind turbine's platform and the vortex-induced vibration of flexible risers.

AUTHOR DECLARATIONS
Conflict of Interest

The authors have no conflicts to disclose.

Author Contributions

Yang Huang: Conceptualization (equal); Data curation (lead); Formal analysis (equal); Investigation (equal); Methodology (lead); Software (equal); Validation (lead); Visualization (lead); Writing – original draft (lead); Writing – review & editing (equal). **Qing Xiao:** Conceptualization (lead); Data curation (equal); Formal analysis (lead); Funding acquisition (lead); Investigation (lead); Methodology (equal); Project administration (lead); Resources (lead); Software (equal); Supervision (lead); Validation (equal); Visualization (equal); Writing – original draft (equal); Writing – review & editing (lead). **Guillermo Idarraga:** Data curation (supporting); Investigation (supporting); Validation (supporting); Writing – review & editing (supporting). **Liu Yang:** Data curation (supporting); Funding acquisition (equal); Investigation (supporting); Project administration (supporting); Supervision (supporting); Validation (supporting); Writing – review & editing (supporting). **Saishuai Dai:** Data curation (supporting); Investigation (supporting); Methodology (supporting); Validation (supporting); Writing – review & editing (supporting). **Frahad Abad:** Data curation (supporting); Investigation (supporting);

Validation (supporting); Writing – review & editing (supporting). **Feargal Brennan:** Funding acquisition (equal); Investigation (supporting); Project administration (supporting); Supervision (supporting). **Saeid Lotfian:** Conceptualization (supporting); Investigation (supporting).

DATA AVAILABILITY

The data that support the findings of this study are available from the corresponding author upon reasonable request.

REFERENCES

Abdelrhman, M. A., "Modeling coupling between eelgrass *Zostera marina* and water flow," Mar. Ecol. Prog. Ser. **338**, 81–96 (2007).

Algie, C., Fleming, A., and Ryan, S., "Experimental and numerical modelling of the Bombora wave energy converter," in *3rd Asian Wave and Tidal Energy Conference* (AWTEC, 2016), Vol. 2, pp. 719–725.

Algie, C., Ryan, S., and Fleming, A., "Predicted power performance of a submerged membrane pressure-differential wave energy converter," Int. J. Mar. Energy **20**, 125–134 (2017).

Ancellin, M., Dong, M., Jean, P., and Dias, F., "Far-field maximal power absorption of a bulging cylindrical wave energy converter," Energies **13**(20), 5499 (2020).

Anssari-Benam, A. and Bucchi, A., "A generalised neo-Hookean strain energy function for application to the finite deformation of elastomers," Int. J. Non-Linear Mech. **128**, 103626 (2021).

AWS, See https://www.awsocean.com/multi-cell-wave-power for "AWS-III multi-cell wave power generator (2023)" accessed May 15, 2023.

Babarit, A., Singh, J., Mélis, C., Wattez, A., and Jean, P., "A linear numerical model for analysing the hydroelastic response of a flexible electroactive wave energy converter," J. Fluids Struct. **74**, 356–384 (2017).

Barree, R. D. and Conway, M. W., "Beyond beta factors: A complete model for Darcy, Forchheimer, and trans-Forchheimer flow in porous media," in *SPE Annual Technical Conference and Exhibition* (OnePetro, 2004).

Bazilevs, Y., Takizawa, K., and Tezduyar, T. E., *Computational Fluid-Structure Interaction: Methods and Applications* (John Wiley & Sons, 2013).

Berberović, E., van Hinsberg, N. P., Jakirlić, S., Roisman, I. V., and Tropea, C., "Drop impact onto a liquid layer of finite thickness: Dynamics of the cavity evolution," Phys. Rev. E **79**(3), 036306 (2009).

Bungartz, H. J., Lindner, F., Gatzhammer, B., Mehl, M., Scheufele, K., Shukaev, A., and Uekermann, B., "preCICE–a fully parallel library for multi-physics surface coupling," Comput. Fluids **141**, 250–258 (2016).

Causin, P., Gerbeau, J. F., and Nobile, F., "Added-mass effect in the design of partitioned algorithms for fluid–structure problems," Comput. Methods Appl. Mech. Eng. **194**(42–44), 4506–4527 (2005).

Chaplin, J. R., Farley, F., Kurniawan, A., Greaves, D., and Hann, M., "Forced heaving motion of a floating air-filled bag," in Proceedings of the 30th International Workshop on Water Waves and Floating Bodies, Bristol, UK, 2015.

Chaplin, J. R., Heller, V., Farley, F. J. M., Hearn, G. E., and Rainey, R. C. T., "Laboratory testing the Anaconda," Philos. Trans. R. Soc., A **370**(1959), 403–424 (2012).

Chourdakis, G., Schneider, D., and Uekermann, B., "OpenFOAM-preCICE: Coupling OpenFOAM with external solvers for multi-physics simulations," OpenFOAM. J. **3**, 1–25 (2023).

Collins, I., Contino, M., Marano, C., Masters, I., and Hossain, M., "On the influence of time-dependent behaviour of elastomeric wave energy harvesting membranes using experimental and numerical modelling techniques," Eur. J. Mech., A: Solids **98**, 104895 (2023).

Collins, I., Hossain, M., Dettmer, W., and Masters, I., "Flexible membrane structures for wave energy harvesting: A review of the developments, materials and computational modelling approaches," Renewable Sustainable Energy Rev. **151**, 111478 (2021).

de Boer, A., van Zuijlen, A. H., and Bijl, H., "Comparison of conservative and consistent approaches for the coupling of non-matching meshes," Comput. Methods Appl. Mech. Eng. **197**(49–50), 4284–4297 (2008).

Dean, R. G. and Dalrymple, R. A., *Water Wave Mechanics for Engineers and Scientists* (World Scientific Publishing Company, 1991), Vol. 2.

Degroote, J., Bathe, K. J., and Vierendeels, J., "Performance of a new partitioned procedure versus a monolithic procedure in fluid–structure interaction," Comput. Struct. **87**(11–12), 793–801 (2009).

Dettmer, W. G., Kadapa, C., and Perić, D., "A stabilised immersed boundary method on hierarchical b-spline grids," Comput. Methods Appl. Mech. Eng. **311**, 415–437 (2016).

Dettmer, W. G., Lovrić, A., Kadapa, C., and Perić, D., "New iterative and staggered solution schemes for incompressible fluid-structure interaction based on Dirichlet-Neumann coupling," Int. J. Numer. Methods Eng. **122**(19), 5204–5235 (2021).

Dettmer, W. and Perić, D., "A computational framework for fluid–structure interaction: Finite element formulation and applications," Comput. Methods Appl. Mech. Eng. **195**(41–43), 5754–5779 (2006).

Dhondt, G., Calculix Crunchix User's Manual Version 2.12, Munich, Germany, 2017.

Falnes, J., *Ocean Waves, Oscillating Systems: Linear Interactions Including Wave-Energy Extraction* (Cambridge University Press, Cambridge, UK, 2004).

Farhat, C., Rallu, A., Wang, K., and Belytschko, T., "Robust and provably second-order explicit–explicit and implicit–explicit staggered time-integrators for highly non-linear compressible fluid–structure interaction problems," Int. J. Numer. Methods Eng. **84**(1), 73–107 (2010).

Farley, F. J. M., and Rainey, R. C. T., U.S. Patent No. 7,980,071 (U.S. Patent and Trademark Office, Washington, DC, 2011).

Farley, F. J. M., Rainey, R. C. T., and Chaplin, J. R., "Rubber tubes in the sea," Philos. Trans. R. Soc., A **370**(1959), 381–402 (2012).

Förster, C., Wall, W. A., and Ramm, E., "Artificial added mass instabilities in sequential staggered coupling of nonlinear structures and incompressible viscous flows," Comput. Methods Appl. Mech. Eng. **196**(7), 1278–1293 (2007).

Haelterman, R., Bogaers, A. E., Scheufele, K., Uekermann, B., and Mehl, M., "Improving the performance of the partitioned QN-ILS procedure for fluid–structure interaction problems: Filtering," Comput. Struct. **171**, 9–17 (2016).

Higuera, P., Lara, J. L., and Losada, I. J., "Realistic wave generation and active wave absorption for Navier–Stokes models: Application to OpenFOAM®," Coastal Eng. **71**, 102–118 (2013).

Higuera, P., Lara, J. L., and Losada, I. J., "Three-dimensional interaction of waves and porous coastal structures using OpenFOAM®. Part I: Formulation and validation," Coastal Eng. **83**, 243–258 (2014a).

Higuera, P., Lara, J. L., and Losada, I. J., "Three-dimensional interaction of waves and porous coastal structures using OpenFOAM®. Part II: Application," Coastal Eng. **83**, 259–270 (2014b).

Huang, Y., Xiao, Q., Idarraga, G., Yang, L., Dai, S., Ahad, F., Brennan, F., and Lotfian, S., "Numerical analysis of flexible tube wave energy converter using CFD-FEA method," in *International Conference on Offshore Mechanics and Arctic Engineering* (American Society of Mechanical Engineers, 2023).

Jasak, H., "Error analysis and estimation for the finite volume method with applications to fluid flows," Ph.D. thesis (Imperial College, University of London, 1996).

Jasak, H., Jemcov, A., and Tukovic, Z., "OpenFOAM: A C++ library for complex physics simulations," in Proceedings of the International Workshop on Coupled Methods in Numerical Dynamics **1000**, 1–20 (2007).

Jean, P., Wattez, A., Ardoise, G., Melis, C., Van Kessel, R., Fourmon, A., and Queau, J. P., "Standing wave tube electro active polymer wave energy converter," Proc. SPIE **8340**, 83400C (2012).

Jiang, L., Betts, A., Kennedy, D., and Jerrams, S., "Eliminating electromechanical instability in dielectric elastomers by employing pre-stretch," J. Phys. D **49**(26), 265401 (2016).

Kadapa, C., Dettmer, W. G., and Perić, D., "A stabilised immersed framework on hierarchical b-spline grids for fluid-flexible structure interaction with solid–solid contact," Comput. Methods Appl. Mech. Eng. **335**, 472–489 (2018).

Kelley, R., David, O., Yi-Hsiang, Y., Adam, K., Nathan, T., Dominic, F., Jorge, L., Jeff, G., and Salman, H. (2022). "WEC-Sim (Version v5.0.1)," Zenodo. https://doi10.5281/zenodo.7121186.

Kelly, M., Boerner, T., and Alam, M. R., "Modeling comparison of flexible-inflatable and rigid small-scale heaving wave energy converters," in ASME 41st International Conference on Ocean, Offshore and Arctic Engineering, 2022.

King, A., Algie, C., Ryan, S., and Ong, R., "Modelling of fluid structure interactions in submerged flexible membranes for the bombora wave energy converter," in 20th Australasian Fluid Mechanics Conference, Perth, Australia, 2016.

Kurniawan, A., Chaplin, J. R., Greaves, D. M., and Hann, M., "Wave energy absorption by a floating air bag," J. Fluid Mech. **812**, 294–320 (2017).

Küttler, U. and Wall, W. A., "Fixed-point fluid–structure interaction solvers with dynamic relaxation," Comput. Mech. **43**(1), 61–72 (2008).

Lachaud, J. and Mansour, N. N., "Porous-material analysis toolbox based on OpenFOAM and applications," J. Thermophys. Heat Transfer **28**(2), 191–202 (2014).

Leighton, S., Algie, C., and Ryan, S. K., U.S. Patent No. 10,883,471 (U.S. Patent and Trademark Office, Washington, DC, 2021).

Li, B., Chen, H., Qiang, J., Hu, S., Zhu, Z., and Wang, Y., "Effect of mechanical pre-stretch on the stabilization of dielectric elastomer actuation," J. Phys. D **44**(15), 155301 (2011).

Li, X. and Xiao, Q., "A numerical study on an oscillating water column wave energy converter with hyper-elastic material," Energies **15**(22), 8345 (2022).

Li, X., Xiao, Q., Zhou, Y., Ning, D., Incecik, A., Nicoll, R., and Campbell, D., "Coupled CFD-MBD numerical modeling of a mechanically coupled WEC array," Ocean Eng. **256**, 111541 (2022).

Liao, Z., Hossain, M., Yao, X., Navaratne, R., and Chagnon, G., "A comprehensive thermo-viscoelastic experimental investigation of Ecoflex polymer," Polym. Test. **86**, 106478 (2020).

Lighthill, J., Waves in Fluids (Cambridge University Press, Cambridge, UK, 2001).

Lindner, F., Mehl, M., and Uekermann, B., "Radial basis function interpolation for black-box multi-physics simulations," in Proceedings of the VII International Conference on Computational Methods for Coupled Problems in Science and Engineering, 2017.

Liu, Y., Xiao, Q., Incecik, A., and Peyrard, C., "Aeroelastic analysis of a floating offshore wind turbine in platform-induced surge motion using a fully coupled CFD-MBD method," Wind Energy **22**(1), 1–20 (2019).

Liu, Y., Xiao, Q., Incecik, A., Peyrard, C., and Wan, D., "Establishing a fully coupled CFD analysis tool for floating offshore wind turbines," Renewable Energy **112**, 280–301 (2017).

Luhar, M. and Nepf, H. M., "Flow-induced reconfiguration of buoyant and flexible aquatic vegetation," Limnol. Oceanogr. **56**(6), 2003–2017 (2011).

Luo, Y., Xiao, Q., and Shi, G., "A fluid–structure interaction study on a bionic fish fin with non-uniform stiffness distribution," J. Offshore Mech. Arct. Eng. **142**(5), 051902 (2020a).

Luo, Y., Xiao, Q., Shi, G., Pan, G., and Chen, D., "The effect of variable stiffness of tuna-like fish body and fin on swimming performance," Bioinspiration Biomimetics **16**(1), 016003 (2020b).

Luo, Y., Xiao, Q., Shi, G., Wen, L., Chen, D., and Pan, G., "A fluid–structure interaction solver for the study on a passively deformed fish fin with non-uniformly distributed stiffness," J. Fluids Struct. **92**, 102778 (2020c).

Martins, P. A. L. S., Natal Jorge, R. M., and Ferreira, A. J. M., "A comparative study of several material models for prediction of hyperelastic properties: Application to silicone-rubber and soft tissues," Strain **42**(3), 135–147 (2006).

Masarati, P., Morandini, M., Quaranta, G., and Mantegazza, P., "Open-source multibody analysis software," in Multibody Dynamics 2003, IDMEC/IST, Lisbon, Portugal, edited by J. A. C. Ambrósio, 1-4 July 2003.

Mcdonald, A., Xiao, Q., Forehand, D., and Costello, R., "Linear analysis of fluid-filled membrane structures using generalised modes," in Proceedings of the 13th European Wave and Tidal Energy Conference, 2019.

McDonald, A., Xiao, Q., Forehand, D., Smith, H., and Costello, R., "Initial development of a generic method for analysis of flexible membrane wave energy converters," in Advances in Renewable Energies Offshore: Proceedings of the 3rd International Conference on Renewable Energies Offshore (RENEW 2018), Lisbon, Portugal (CRC Press, 2018), p. 333.

Mehl, M., Uekermann, B., Bijl, H., Blom, D., Gatzhammer, B., and Van Zuijlen, A., "Parallel coupling numerics for partitioned fluid–structure interaction simulations," Comput. Math. Appl. **71**(4), 869–891 (2016).

Mendes, A. C., Braga, F. P., Paredes, L. M. A., and Chaplin, J. R., "Performance assessment of the ANACONDA WEC in regular waves at 1:50 model scale," in ASME 36th International Conference on Ocean, Offshore and Arctic Engineering (American Society of Mechanical Engineers, 2017), Vol. 57786.

Montiel, F., Bonnefoy, F., Ferrant, P., Bennetts, L. G., Squire, V. A., and Marsault, P., "Hydroelastic response of floating elastic discs to regular waves. Part 1. Wave basin experiments," J. Fluid Mech. **723**, 604–628 (2013).

Mooney, M., "A theory of large elastic deformation," J. Appl. Phys. **11**(9), 582–592 (1940).

Moretti, G., Malara, G., Scialò, A., Daniele, L., Romolo, A., Vertechy, R., and Arena, F., "Modelling and field testing of a breakwater-integrated U-OWC wave energy converter with dielectric elastomer generator," Renewable Energy **146**, 628–642 (2020).

Moretti, G., Rosati Papini, G. P., Daniele, L., Forehand, D., Ingram, D., Vertechy, R., and Fontana, M., "Modelling and testing of a wave energy converter based on dielectric elastomer generators," Proc. R. Soc. A **475**(2222), 20180566 (2019).

Pedley, T. J., The Fluid Mechanics of Large Blood Vessels (Cambridge University Press, Cambridge, 1980).

Rivlin, R. S., "Large elastic deformations of isotropic materials IV. Further developments general theory," Philos. Trans. R. Soc., A **241**(835), 379–397 (1948).

Rosati Papini, G. P., Moretti, G., Vertechy, R., and Fontana, M., "Control of an oscillating water column wave energy converter based on dielectric elastomer generator," Nonlinear Dyn. **92**, 181–202 (2018).

Ryzhakov, P. B. and Oñate, E., "A finite element model for fluid–structure interaction problems involving closed membranes, internal and external fluids," Comput. Methods Appl. Mech. Eng. **326**, 422–445 (2017).

Schäffer, H. A. and Klopman, G., "Review of multidirectional active wave absorption methods," J. Waterway, Port, Coastal, Ocean Eng. **126**(2), 88–97 (2000).

Shabara, M. A. and Abdelkhalik, O., "Dynamic modeling of the motions of variable-shape wave energy converters," Renewable Sustainable Energy Rev. **173**, 113070 (2023).

Shabara, M. A., Zou, S., and Abdelkhalik, O., "Numerical investigation of a variable-shape buoy wave energy converter," in ASME 40th International Conference on Ocean, Offshore and Arctic Engineering, 2021.

Sirigu, S. A., Bonfanti, M., Begovic, E., Bertorello, C., Dafnakis, P., Giorgi, G. et al., "Experimental investigation of the mooring system of a wave energy converter in operating and extreme wave conditions," J. Mar. Sci. Eng. **8**(3), 180 (2020).

Steinmann, P., Hossain, M., and Possart, G., "Hyperelastic models for rubber-like materials: Consistent tangent operators and suitability for Treloar's data," Arch. Appl. Mech. **82**, 1183–1217 (2012).

Tian, F. B., Dai, H., Luo, H., Doyle, J. F., and Rousseau, B., "Fluid–structure interaction involving large deformations: 3D simulations and applications to biological systems," J. Comput. Phys. **258**, 451–469 (2014).

Toland, J. F., "Stokes waves," Topol. Methods Nonlinear Anal. **7**, 1–48 (1996).

Uekermann, B., Bungartz, H. J., Yau, L. C., Chourdakis, G., and Rusch, A., "Official preCICE adapters for standard open-source solvers," in Proceedings of the 7th GACM Colloquium on Computational Mechanics for Young Scientists from Academia, 2017.

Vertechy, R., Fontana, M., Papini, G. R., and Bergamasco, M., "Oscillating-water-column wave-energy-converter based on dielectric elastomer generator," Proc. SPIE **8687**, 86870I (2013).

Wave Venture Ltd, see http://www.wave-venture.com/ for information about Wave Venture TE™ software (2023) (accessed May 15, 2023).

Wei, G. and Kirby, J. T., "Time-dependent numerical code for extended Boussinesq equations," J. Waterw, Port, Coastal, Ocean Eng. **121**(5), 251–261 (1995).

Weller, H. G., "Derivation, modelling and solution of the conditionally averaged two-phase flow equations," OpenCFD Technical Report No. TR/HGW/02 (2002).

Zhang, Y., Zhao, Y., Sun, W., and Li, J., "Ocean wave energy converters: Technical principle, device realization, and performance evaluation," Renewable Sustainable Energy Rev. **141**, 110764 (2021).

Zhou, Y., Xiao, Q., Liu, Y., Incecik, A., Peyrard, C., Li, S., and Pan, G., "Numerical modelling of dynamic responses of a floating offshore wind turbine subject to focused waves," Energies **12**(18), 3482 (2019).

Zhou, Y., Xiao, Q., Peyrard, C., and Pan, G., "Assessing focused wave applicability on a coupled aero-hydro-mooring FOWT system using CFD approach," Ocean Eng. **240**, 109987 (2021).

Zou, S. and Abdelkhalik, O., "A numerical simulation of a variable-shape buoy wave energy converter," J. Mar. Sci. Eng. **9**(6), 625 (2021).